Synchronous Optical and Electrical Measurements of Single DNA Molecules Translocating Through a Solid-State Nanopore

uOttawa

JOSÉ BUSTAMANTE

THESIS SUBMITTED IN PARTIAL FULFILLMENT OF THE REQUIREMENTS

FOR THE DEGREE OF

MASTER OF SCIENCE

in the Faculty of Graduate Studies (Physics)

UNIVERSITY OF OTTAWA

© José Bustamante, Ottawa, Canada, 2015

Para Ana y Ema, desde el fondo de mi alma.

Ahí donde yo vivo, hay una de viejas, y no mueren. No morimos pues, yo también ya soy vieja.

Enma Lucía de Jesus Sevilla Bucheli (1918-2014)

STATEMENT OF ORIGINALITY

The content presented in this thesis is, to the best of the author's knowledge, the product of original work done by the author at the University of Ottawa under the supervision of Professor Vincent Tabard-Cossa.

The majority of the content of Chapters 2 and 3 will be presented for publication under the title:

"*Noise Analysis and Minimization in Nanopore-based Optofluidic Systems for Simultaneous Fluorescence and Electrical Measurements"* by **Bustamante, J.**; and Tabard-Cossa, V. under preparation for *Review of Scientific Instruments*.

Contributions, not included in this Thesis, the author has made have been submitted for publication under the titles:

"Long passage times of short ssDNA molecules through metallized nanopores fabricated by dielectric breakdown" by Kwok, H.; Waugh, M.; **Bustamante**, J.; Briggs, K.; Tabard-Cossa, V. (2014) *Advanced Functional Materials* doi: 10.1002/adfm.201402468

"*Kinetics of Nanopore Fabrication by Controlled Breakdown of a Dielectric Membrane in Solution"* by Briggs, K.; Charron, M.; Kwok, H.; Le, T.; Chahal, S.; **Bustamante, J.**; Waugh, M.; and Tabard-Cossa, V. (2014) accepted in *Nanotechnology* - special issue on DNA sequencing.

The preliminary results about Localized nanopore fabrication via laser enhanced dielectric breakdown (Chapter 4) are still under investigation, and they will be presented for publication at a later time. An invention disclosure was also submitted.

I had the opportunity to participate in the 58th Biophysical Society Meeting, held in San Francisco CA. in February 2014. I presented a poster entitled:

"Synchronous Optical and Electrical Measurements of single DNA molecules translocating through a solid-state nanopore" by **Bustamante, J.;** Yelle, N.; and Tabard-Cossa, V. Biophysical Society Meeting, February (2014).

As a partial requirement for the degree of Master of Science (Physics) at the University of Ottawa, advances on Synchronous measurements and noise minimization were presented at the Ottawa Carleton Institute of Physics symposium:

Synchronous Optical and Electrical Measurements of Single DNA Molecules Translocating Through a Solid-State Nanopore" by **Bustamante J.** and Tabard-Cossa, V. "Ottawa Carleton Institute of Physics (May 2014).

STATEMENT OF CONTRIBUTIONS

All sample preparation, data acquisition and analysis presented in this thesis were performed by the author. The design of the instrument was done in its majority by the author except for: initial mounting of the microscope and camera, and the design of the microfluidic channels. All the nanopores in used in this work were fabricated by the author. The microfluidic devices were fabricated by the author, with the help during the Fall 2013, of a Coop student, Nick Yelle. The LabView routines used for data acquisition and analysis were versions of codes provided by Prof. Vincent Tabard-Cossa or by Harold Kwok in the T.-Cossa Lab. The LabView routine to acquire the current and voltage from the Axopatch, and the trigger signal from the camera was written with the help of Lukasz Andrzejewski. The nanopore fabrication circuit was designed by Prof. Vincent Tabard-Cossa and Harold Kwok and built by Lukasz Andrzejewski. Figures 1.1, 1.2, 2.1 were reproduced with permissions from the cited source. Figure 1.3, was graciously provided by Prof. Tabard-Cossa. All remaining figures and plots were original work done by the author.

ABSTRACT

Nanopore sensors are emerging as a promising technology for single molecule analysis and polymer sequencing. Traditionally, measurements are taken by monitoring the ionic current through the nanopore, which gives information (e.g. size, shape, charge) about a molecule of interest while it is in the confined geometry of the nanopore. The dynamics of the molecule before the arrival to the nanopore, such as the capture dynamics, or molecular conformation prior to translocation, as well as clogging mechanisms and features of anomalous translocation events, are not assessed by the electrical measurements alone. To study the whole process of nanopore diffusion, capture and passage it is necessary to complement the electrical signal with another detection mode. Particularly, optical visualization of the molecules as they translocate through the nanopore has great potential.

In this Thesis I present the design, construction, optimization and testing of a nanopore-based optofluidic instrument, which uses fluorescence microscopy to visualize individual fluorescently stained DNA molecules as they translocate a solid-state nanopore, while in parallel record the ionic current signal through the pore. The following challenges were overcome to achieve the integration of the optical and electrical systems: (i) the electrical detection system must account for the physical constrains of a wide field fluorescence microscope, and the optical system should in turn not affect the low-noise electrical detection of individual

DNA molecules. The design of the instrument included a microfluidic device, so to position the nanopore within the working distance (<170-μm) of the microscope objective (Chapter 2). (ii) Electrical noise was optimized to a level that is indistinguishable from a standard (with no optics) nanopore system (Chapter 3).

The custom instrument was used to demonstrate: 1) Electrical detection of DNA translocations with a laser light illuminating the nanopore; 2) Optical tracking of DNA capture and translocation dynamics; 3) Synchronization of the optical and electrical signals in preparation for simultaneous detection. In the process of noise optimization, a strong noise coupling between the illumination source and the ionic current was found, characterized and eliminated. Consequently, the noise performance of the custom instrument is the lowest of any other nanopore-based optofluidic systems described in the literature to date. This opens up the way to many new and exciting investigations of polymer translocation dynamics through nanoconfined geometries. Lastly, during the development of this custom instrument, a method to localize the fabrication of a nanopore by controlled dielectric breakdown on a membrane, with a focused laser beam, was discovered.

ACKNOWLEDGEMENTS

Since this project involved so many techniques and methods, it is difficult to keep track of all the persons that taught me all these things I needed to know to accomplish my research objectives. I start by thanking Kyle Briggs, Harold Kwok and Matt Waugh, the members of our group who have patiently answered my endless questions about nanopore fabrication and electrical detection. I will then continue with Radin Tahvildari, from The Godin Lab for helping me learn PDMS-based microfluidic fabrication. All the microfluidic device fabrication was done in Professor Michel Godin's lab, and I would like to thank him for graciously sharing his equipment with us. Professor Ravi Bhardwaj and Dr. Lakshmi Narayan Kallepalli helped us with ideas and equipment to measure the laser stability and to implement the laser beam expander and attenuator. Special thanks also to Professor Joshua Milstein (University of Toronto) for the design of the laser illumination system. Harold Kwok and Lukasz Andrzejewski were always available to help me debug LabView programs. I am very grateful for all these contributions to my work. The funding for the Masters Degree was provided by SENESCYT (Ecuador).

A special note must be made to mention all the patience, tolerance and true support that I have received from Professor Vincent Tabard-Cossa. He directed this work, was constantly present to discuss the many questions that originated along the way and didn't hesitate to come to the lab to try to solve all kinds of experimental problems with me. I appreciate his guidance and admire his tenacity towards research.

I shall also thank the person who has made me smile every morning and endured my bad cooking. The little child who taught me how innocence brings joy to life, is my daughter Ema. I also thank for the tremendous help my family received in several emergencies that we faced during our stay in Canada. Miriam Navarrete, Gabriel Cuesta, Andrea Carrión, Gonzalo Gonzales, Negui Carrera, Alejandro Hernandez, Martha Werner, you all made this possible.

Finally and most importantly, I have been extremely fortunate to share this, among other adventures, with the most beautiful person, my wife Ana. She is the motor of my life, the ultimate motivation to be better and the evidence that nature manifests itself in the forms of intelligence, beauty and love.

CONTENTS

LIST OF FIGURES

LIST OF ACRONYMS

bp	***base pairs***
CLIC	Convex Lens-Induced Confinement
DNA	Deoxyribonucleic acid
DOF	Depth of Focus
dsDNA	double stranded DNA
ITO	Indium Tin Oxide
LPCVD	low-pressure chemical vapour deposition
N.A.	Numerical Aperture
PCR	Polymerase Chain Reaction
PDMS	Polydimethylsiloxane
PSD	Power Spectral Density
PTFE	Polytetrafluoroethylene
PEEK	Polyether Ether Ketone
RIE	Reactive Ion Etching
RNA	Ribonucleic acid
ssDNA	single stranded DNA
λ-DNA	DNA from the bacterial virus Enterobacteria phage λ, 48490 bp long

1 INTRODUCTION

1.1 Nanopore sensors

Nanopore devices are a promising single-molecule technology for the detection and sequencing of biomolecules such as DNA, RNA and proteins. A nanopore is a small aperture, ideally cylindrical, in a thin (5-30nm) strongly insulating membrane. The materials of choice for the thin membrane are silicon nitride or silicon oxide. However, the membrane could also be made of graphene or a polymer[1,2]. Nanopore sensors use the Coulter principle to detect nanometer-sized objects[3]. This simple, intuitive measurement principle can be described as follows. The nanopore is the only fluidic connection between two reservoirs filled with electrolytic solution. Upon the application of an electric field, an ionic flow through the nanopore is initiated. An object passing through the nanopore will cause an alteration in the current through it, depending on properties of the object such as size, shape and charge. By measuring the current through the nanopore as a

function of time with enough sensitivity, one can detect the passage of single molecules and characterize their properties.

Although the field of sequencing is advancing fast, all the sequencing techniques remain costly and time consuming, which prevents medicine from using sequencing of patients on a regular basis. DNA sequencing has a myriad of potentialities both for research and medical purposes. Applications range from early detection of genetically inherited diseases, to the study of mutations, among a myriad of other possibilities.

There are many approaches to sequencing using nanopores, but the main and more promising mechanism relies on the detection of ionic current changes produced by a single base at a time (the sequence could also be determined from a signal resulting from the average of many bases, assuming the signal could be de-convoluted to discern the contribution of each base). This objective implies several challenges.

First, the translocation of DNA is too fast in terms of present temporal resolution to permit standard electronics to resolve a single base. For example, the translocation speed for polyC, polyA and polyU RNA is 2, 20 and 6 μs/nucleotide respectively, in a proteinaceous nanopore[4], which would require a sampling rate of 0.5 μs/sample. At this frequency the noise in solid state nanopores is very high and impedes the detection.

Second, translocation doesn't always maintain a constant speed[5]. The duration, velocity and possibly other features of the translocation dynamics depend on the

initial configuration of the polymer: depending on the entropy of the initial configuration, the polymer will take more or less time to unwind. This phenomenon widens the distribution of translocation times for a given polymer length. Lu et al.[6] have developed a theory that relates the variations of the velocity of the polymer translocating through the nanopore to its initial conformation: the polymer adopts the most entropically favourable configuration in free solution. Depending on the complexity of the configuration, it takes more or less time to unravel through the nanopore. This theory still needs experimental confirmation, but if correct, the velocity variability it suggests must be addressed to achieve the capability of sequencing with solid-state nanopores.

Furthermore, DNA can stick to the walls of the nanopore and remain momentarily stuck. The passage happens in steps, which is undesirable for sequencing purposes[7]. It can also translocate in a stick-slip manner because of diffusion. This phenomenon is observed when the electric field is reduced. Since the molecule feels less force it translocates more slowly. However, diffusion starts to play an important role in the DNA motion at low electric fields and the motion becomes random in one dimension through the pore[8], and DNA analysis is more complicated.

Third, multiple bases reside at the pore at a given time. Even if we consider an idealized nanopore in an infinitely thin membrane (real membranes are 5-30nm thick) the electric field is very strong at the entrance of the pore, so the detection region extends to one channel diameter on each side. Since the diameter of the nanopore has to be big enough to at least permit the passage of single stranded

DNA (ssDNA) (~1.5nm), there is a minimum 3nm region of detection. The distance between bases is ~0.3nm, so many bases reside in the nanopore at a given instant even in the idealized infinitely thin nanopore. Thus, the current reading results from an average of multiple bases[9].

Challenges to sequencing do not only arise from the difficulties of detecting single bases, there are also a number of problems related to the yield on the fabrication of nanopores. Nanopores are fabricated with a focused beam of ions or electrons.[10] The high-energy beam removes material and creates a nanopore, but the equipment to create a focused beam is expensive. Also, the size and shape of nanopores is not reliably controlled. Thermal fluctuations of the nanopore fabrication instrument cause the beam to slowly drift and nanopores are often elongated. Furthermore, nanopores are not easily wetted after fabrication, and some of them display high electrical noise once they are wetted.

A final challenge to nanopore sequencing is presented by the fact that there are a number of anomalous events[11,12] in every DNA translocation experiment, which cannot be attributed accurately to DNA passage, or to collisions of the DNA with the nanopore mouth, or any other type of interaction. A nanopore is a very good sensor to measure objects in the pore and it precisely tells the conformation of the polymer inside the nanopore (unfolded, and one or more folds). However, it provides no information on the shape, conformation or location of the polymer before translocation. Thus, this information is unknown to date. The anomalous translocation events are readily ignored and left for speculation, since there is no way to accurately assess them using electrical detection alone.

1.2 Motivation

The challenges described above highlight the need for development of a new tool to further investigate the process of capture, unfolding and translocation of polymers through nanopores. In particular, the nanopore field stands to benefit significantly from further study of the correlation between translocation time and initial polymer configuration. This is one of the central motivations of this work: I would like to experimentally verify this correlation, study the passage of DNA through a nanopore optically and eventually try to find potential solutions for velocity variations due to differences in the initial conformation.

Thus, I set out to build an instrument capable of interrogating a solid-state nanopore system with regard to: 1) the correlation between initial polymer conformation and distribution of translocation times, 2) the origin of anomalous events, and 3) the dynamics of clogged pores. In this work, I have developed a general tool to assess optically all these aspects of a nanopore experiment: we can measure the motion of DNA molecules in free solution and study the capture and translocation process. I have decided to explore a regime where the nanopores have a diameter that approaches the diameter of DNA, that is 3 to 10nm, which is necessary to produce a clear electrical detection of DNA molecules.

The capabilities of the tool I developed were enhanced by a nanopore fabrication method recently developed by Kwok *et al.*[11] in our laboratory. The method basically consists of applying a very strong electric field through a membrane immersed in electrolyte solution (with no pore yet) and monitoring the leaking

current (by a form of tunnelling mechanism) through it. The current passing through the membrane creates electron traps (defects) in the substrate, which further assist the tunnelling of more current. This self-enhanced process concludes with the localization of the tunnelling current on one spot, and eventually material is removed, creating a single nanopore. The nanopore fabrication event is signalled by an abrupt spike in the current trace, which indicates breakdown and the onset of ionic conduction. Using this method, nanopore location on the membrane is random.

In addition to fabrication, there is a technique to enlarge pores until a specific diameter is reached. The diameter of the pore can be controlled by a series of pulses as previously described in [13]. To summarize the method: high voltage pulses are applied to the pore while electrical current is monitored. An increase of current corresponds to an increase in the pore's size. The yield of this method is very good (>90%) and there is a variety of techniques to control noise performance[13]. The exact mechanism of this fabrication process is not yet fully understood, and the method itself needs further investigation.

Now that the tool is functional, I have discovered that it can be used for other purposes as well. Besides simply observing the membrane as a nanopore is fabricated by dielectric breakdown, I can force the nanopore to form in a particular location by locally enhancing conduction using a focused laser beam. The method of localized fabrication via laser enhanced dielectric breakdown. These optical capabilities, along with the capacity to detect translocation electrically, offer the

possibility of tackling many open questions. The optical technique employed to optically visualize DNA molecules in the tool used in this work is fluorescence microscopy. I present a brief introduction next.

1.3 Fluorescence Microscopy

Fluorescence microscopy is a microscopy technique designed to increase the contrast of a selected target analyte[14]. It relies on the ability of certain molecules (fluorophores) to absorb a photon of a particular energy, and reemit a lower energy photon. The excitation light can be filtered away with a dichroic mirror, so that only the emission light is collected into the eyepiece, or digital camera(Figure 1.1). All light from the illumination source carrying no information is discarded. This gives a major advantage in terms of contrast, since only selected spots from the sample will be emitting the light collected to form the final image. Fluorophores can be designed to attach to a specific sample site, allowing the targeting of cells, organelles, or individual molecules such as proteins, DNA or RNA.

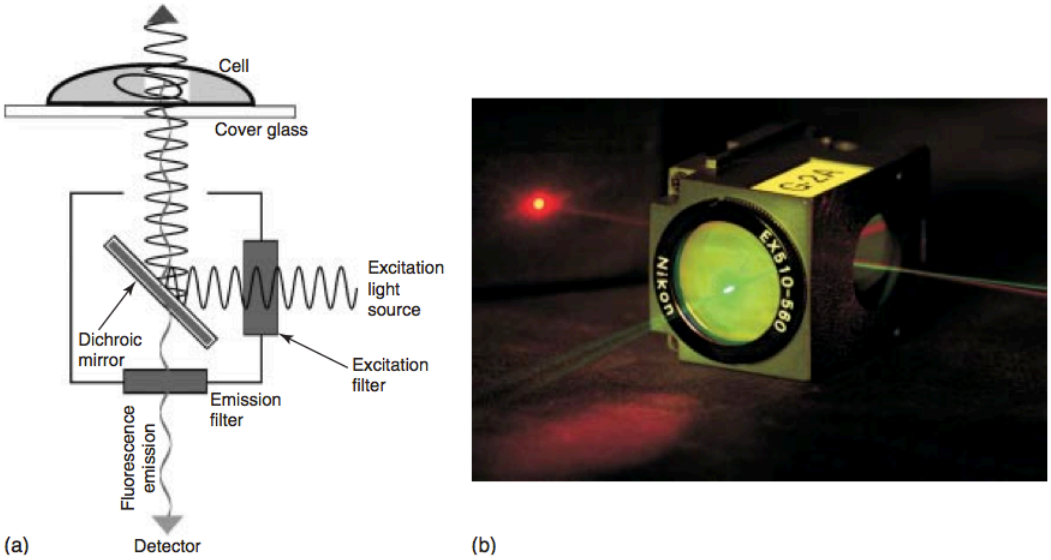

Figure 1.1 Principle of fluorescence microscopy. Illumination light is filtered by the excitation filter then reflected on a dichroic mirror and directed to the sample. In the sample, fluorophores absorb photons and reemit lower-energy photons. The lower-energy light does not reflect on the mirror and passes straight to the eyepiece or camera. b) The element composed from filters and dichroic mirror is called a filter cube. Reproduced with permission from [14].

A schematic diagram of a fluorescence microscope is shown in Figure 1.2. The advantage of this system is that the illumination light passes through the objective to reach the sample (fluorescence that uses the objective to illuminate and to visualize the sample at the same time is called epifluorescence). Excess excitation light is transmitted and not collected back in the microscope (as it would be if the condenser were directly oriented towards the objective.) The fraction of light that is reflected off the sample is filtered by the dichroic mirror, and only the light emitted by the fluorophores is permitted to pass through the mirror to reach the camera. When a wide spectrum excitation source is used, such as a mercury lamp, the excitation light is selected through the use of an excitation filter, which eliminates all the light except for the colour that will excite the fluorophores. This

filter is not necessary if the light source is monochromatic like a laser. To assure that only the emission light is collected, an emission filter is also used. The resulting image can either go to the eyepiece or to a digital camera, depending on the position of a mirror.

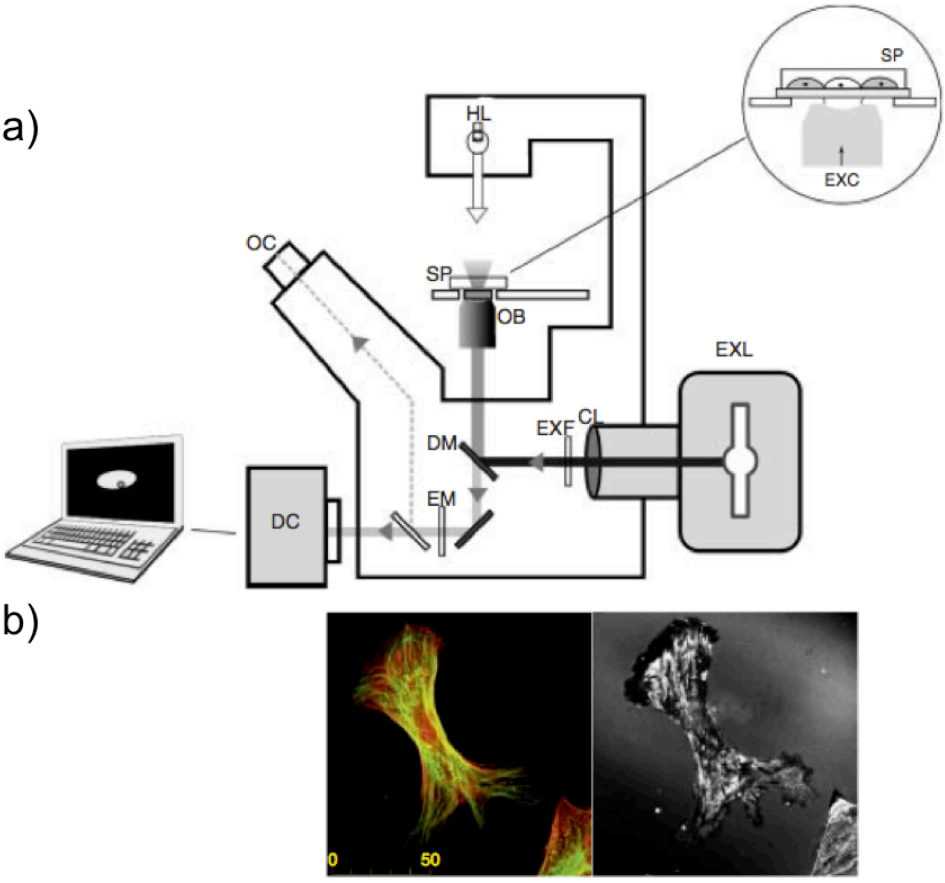

Figure 1.2 Principle of operation of a fluorescence microscope. a) Schematic diagram of an inverted fluorescence microscope similar to the one I used. Following the light path we have: the excitation light source EXL, the condenser lens CL, the excitation filter EXF (which eliminates all colours but the excitation wavelength,) and the dichroic mirror DM (which reflects the excitation light and lets the emitted light pass.) Light focuses through the objective OB and is collected back through the same lens. The emitted light passes through the dichroic mirror and is further filtered by the emission filter EM. A mirror is used to form the final image on a digital camera DC or an ocular (eyepiece) OC. b) Example images obtained with fluorescence microscopy. In this case we see the inner structures of the cell, namely microtubules (green) and actin fibres (red). On the right there is

an image of the same cell obtained from a reflected light configuration. Reproduced with permission from [14].

Fluorescence microscopy can achieve a sufficient signal to noise ratio to visualize single molecules. Their image will be diffraction-limited, but their location can be fully determined. In our case, fluorescence microscopy is a very attractive technique, since DNA can be coated with a fluorophore and a single DNA molecule can be visualized.

One disadvantage of wide field fluorescence microscopy is that illumination volume can be very large with the effect of illuminating many molecules and losing contrast. In our case, we can minimize illumination volume by incorporating shallow microfluidic channels to avoid the illumination of an excessive number of molecules.

Other techniques exist to reduce illumination volume, such as Total Internal Fluorescence (TIRF) or Confocal Microscopy, but they have more technical difficulties in this context than does wide field fluorescence in combination with microfluidics. It should be noted that other wide field microscopy techniques with reduced illumination volumes and potential for implementation in a nanopore setup are being developed, such as Convex Lens-Induced Confinement (CLIC) microscopy [15]. In this case, researchers use confinement as a treatment to bring the molecule to a known configuration before translocation, which should drastically reduce the variations in translocation time for identical molecules[16].

1.4 Review of previous work combining fluorescence and electrical detection through a nanopore

Other groups have also implemented an optical channel with fluorescence microscopy within a nanopore setup. Soni *et al.*[17] reported a platform to perform a synchronous optical and electrical detection of biomolecules traversing through a solid-state nanopore. They used Total Internal Reflection Fluorescence (TIRF) to reduce the optical background and achieve a good optical signal to noise ratio. They used 421 base pairs (bp) DNA fragments, which were labelled with Alexa647 fluorophores by incorporation of amine modified-thymine during Polymerase Chain Reaction (PCR). The group also showed a high correlation between the optical intensity spikes of a 3x3 pixel region and blockages in the electrical current trace, demonstrating the feasibility of detecting DNA and DNA-protein complexes both electrically and optically. This instrument was then used to sequence hybridized DNA, with a two colour scheme.[18] It is interesting to note that they labelled their DNA covalently so that the dye molecules will stay bound to the DNA in any electrolyte concentration. Electrostatically bound dyes (such as YOYO-1, SYBR GREEN, BOBO, TOTO) need a low electrolyte concentration, otherwise the salt ions screen all electrostatic interactions and the positive dye is detached from negative DNA.

Despite difficulties encountered in electrical and optical detection in low electrolyte solutions[19], some groups have succeeded in simultaneous electrical and optical detection of DNA. Kurz *et al.* [20] reported such detection. Nevertheless their electrical signals are barely above the noise level. Their signal to noise ratio is approximately 0.5 for linear DNA. The fundamental problem when working at such

low salt concentration levels is that instead of current blockages one gets current increases since the DNA is more charged than the bulk solution. However, when DNA is labelled with a charged dye, its total effective charge might change substantially.

Some other researchers have investigated nanopores with a purely optical approach. Ando *et al.*[21] measure fluorescence and look at the motion of DNA close to a nanopore. It is worth mentioning that they use pores with a ~100nm diameter, so that their results are in a different regime from what is usually studied for DNA sequencing (d = 3-10nm). Their measurements give some insights into clogging: they find the clogging probability increases as the voltage applied increases. They mention also that once the pore clogged, it did not unclog despite the high voltage applied to try to unclog it. This behaviour contrasts with the technique Beamish *et al.*[13] use to resuscitate clogged pores. The difference might be due to the YOYO-1 dye that interferes with interactions between DNA and the pore and makes it more difficult to remove DNA clogging the pore.

1.5 Electrical detection of single DNA molecules through nanopores

Once a nanopore is created and it is enlarged to an appropriate size, a fabrication circuit is replaced with a low noise current amplifier (Axopatch 200B, Molecular devices) to perform electrical detection of single molecules. I will review the instrumentation in detail in chapter 2.

The conductance through a nanopore can be very well described by the equation [19]

$$G_{pore} = \frac{\pi d_{pore}^2}{4\, L_{pore}} \left[(\mu_{\mathrm{K}} + \mu_{\mathrm{Cl}}) n_{\mathrm{KCl}} e + \mu_{\mathrm{K}} \frac{4\alpha}{d_{pore}} \right] \quad (1.1)$$

where L_{pore} is the length of the nanopore, d_{pore} is the diameter of the pore, μ_K and μ_{Cl} are the mobilities of the positive and negative ion species in the solution (K, and Cl), e is the fundamental charge, and α is the surface charge density. Equation 1.1 has two terms: the first arises from the conductance of the bulk solution inside the pore; the second term is related to the surface charge inside the pore, it depends only on the ion species that screen the negative charge of the silicon nitride. Equation 1.1 is also used to calculate the effective diameter of the pore from the conductance measurement in high salt (>1M KCl), using the measured value of the conductivity of the electrolyte solution, assuming the pore length being equal to the nominal membrane thickness and ignoring surface effects.

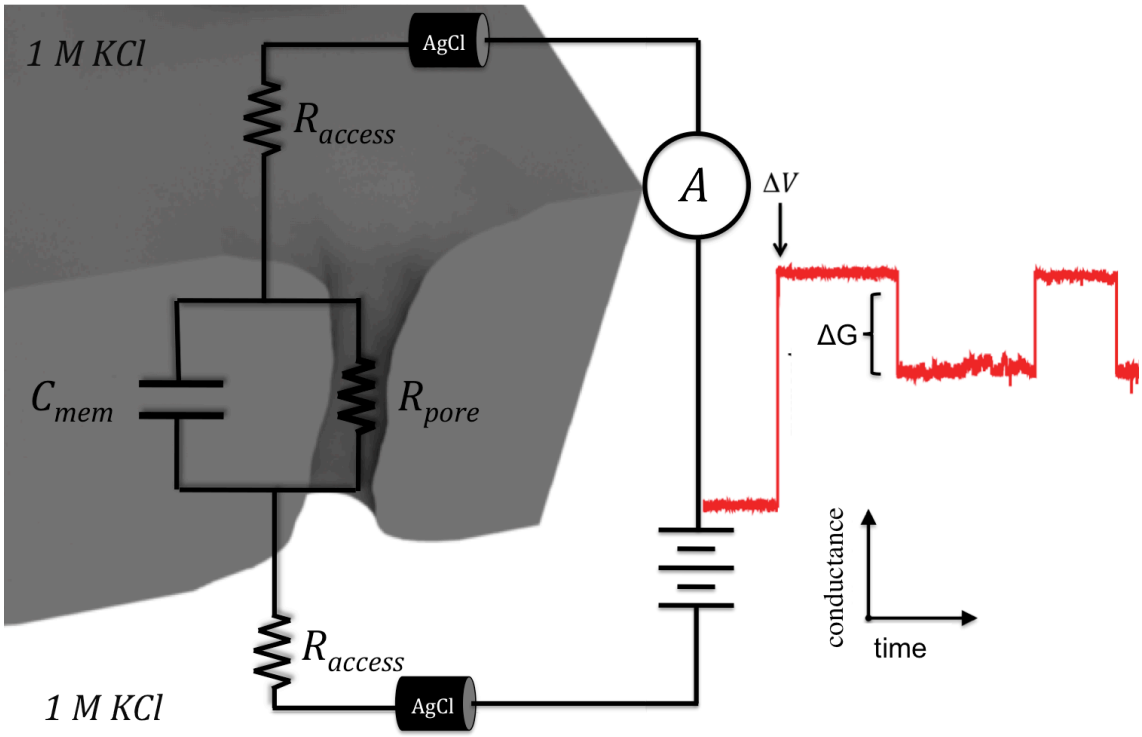

Figure 1.3 Schematic representation of a nanopore and its equivalent circuit. To detect DNA, a voltage is applied across the nanopore and we monitor the current passing through it. The open conductance is given by equation 1.1 and the change in conductance ΔG is observed as a molecule translocates through the pore.

Upon entrance of a DNA molecule in the pore, a change on the conductance can be observed according to the expression

$$\Delta G = -\frac{1}{L_{pore}}\left(\pi r_{\mathrm{DNA}}^2(\mu_K + \mu_{Cl})n_{KCl}e - \mu_K^* q_{l,DNA}^*\right) \tag{1.2}$$

where ΔG is the change in conductane, L is the length of the nanopore, r_{DNA} is the DNA radius, μ_K, μ_{Cl} are the electrophoretic mobilities of K^+ and Cl^-, n_{KCl} is the number density of electrolyte ions, e is the fundamental charge, μ_K^* is the effective electrophoretic mobility of potassium on the DNA surface and $q_{l,DNA}^*$ is the effective DNA surface charge per unit length.[19] Equation 1.2 takes into account two separate

phenomena: the first term stands for the blockade produced by the DNA, which reduces the effective area of the pore and hence the conductance. The second term stands for the charge of the DNA backbone counterions, which induce a current as they are inserted in the pore. The second term becomes important when the concentration of the bulk solution is lower than ~400mM. In this regime, the DNA contributes more to the current than the bulk solution, since it carries more charge than an equal volume of the solution. Thus a conductance increase is observed as opposed to a blockage. There is a concentration for which a zero conductance change is observed, where both effects cancel each other and DNA is undetectable.

At high enough concentrations (> 1M) the second term in equation 1.2 can be safely neglected and only the bulk contribution is taken into account[22]. Setting the second term equal to zero, equation 1.2 becomes:

$$\Delta G = -\frac{1}{L_{pore}}\pi r_{\mathrm{DNA}}^2(\mu_K + \mu_{Cl})n_{KCl}e = -\frac{\sigma\pi d_{DNA}^2}{4L_{pore}} \qquad (1.3)$$

where $\sigma = (\mu_K + \mu_{Cl})n_{KCl}e$ is the conductivity of the solution, d_{DNA} is the diameter of DNA, and L is the length of the pore. For our particular application we would like to detect DNA translocation events for long molecules (>10kbp) so the time resolution needs to allow us to detect events on the order of 100μs to 700μs[23]. This can be accomplished with a sampling frequency of 100kHz, that is to say one sample every 10 μs. However the noise is proportional to the bandwidth (see Chapter 3), so I will eliminate the high frequency noise with a 4-pole Bessel filter at a cut-off frequency of 10kHz. The edges of the blockade events will be rounded, since the high frequency components of the square pulse are eliminated. The rise

time τ_{rise}, defined as the time the signal takes to rise from 10% of the blockage to 90% of it, can be calculated by[24]

$$\tau_{rise} \simeq \frac{0.35}{f_c} \tag{1.4}$$

which results in 35μs for $f_c = 10kHz$. Therefore, the expected translocation time, 100 to 700 μs >> τ_{rise} so, the optofluidic instrument should be able to detect DNA electrically.

The time resolution of the digital camera, however, is much lower. The camera at full frame can take up to 30 frames per second (fps), although the parameters can be adjusted for it to work at ~8000fps (1 frame every 125μs). The increase in temporal resolution has a spatial resolution cost. The camera needs to work with a reduced frame that might not capture accurately the conformation information. Also, the light collected in such a short period of time might not be able to form an image. In any case, the expectation is to have one frame before translocation, and one after. The temporal resolution of the camera is not sufficient to have photographs of the whole translocation process.

1.6 Outline

In this opening chapter I have described the challenges in the nanopore field and the necessity to study translocation processes with new tools. The advantages of an instrument that combines electrical detection with optical fluorescence imaging of DNA molecules translocating through a nanopore were exposed. I have also exposed some of the basics of the techniques necessary to implement such an

instrument, namely, electrical detection of molecules through nanopores and fluorescence microscopy.

I believe that this instrument will give us insight into what happens with polymers before and after translocation through a pore. The main challenges I have faced are the integration of the optical and electrical systems so that they do not interfere with each other: the optical system should not increase electrical noise so as to jeopardize the electrical measurements; and the electrical system should be implemented within the geometrical restrictions of wide field fluorescence microscopy.

In chapter 2, I will review the instrumentation for electrical and optical detection and how it deviates from the instrumentation of a purely electrical nanopore setup. Then I will present the physical design of the instrument with a discussion of the relevant arguments that were taken into account during the construction. Almost every part evolved through multiple versions, but we will review just the final functional version of the instrument. The most important criterion that I took into account during the construction of the instrument was electrical noise optimization.

In Chapter 3 we will review all the noise sources of a nanopore experiment and how they are affected when an optical system is introduced. I will then describe the strategies employed to minimize the noise and bring the instrument to have an acceptable signal to noise ratio.

In Chapter 4, I will present the preliminary results obtained with the instrument. To be specific, I will focus on electrical detection of DNA molecules, optical detection of DNA molecules in free solution and the observation of optical translocation through a nanopore. An experiment that proves that DNA can be detected electrically with all the optical system working will be shown, demonstrating that noise levels have been reduced to the point where the instrument can fulfil its purpose.

In the outlook section I will then describe the method of localized nanopore fabrication via dielectric breakdown. Finally, the challenges I anticipate in obtaining simultaneous optical and electrical detection will be discussed and potential solutions proposed.

2 Instrumentation for Simultaneous Fluorescence and Electrical Measurements

In this chapter I will describe the custom instrument that I designed and assembled, taking into account all necessary technical considerations to build it. I will first describe the electrical system to make ionic current measurements through solid-state nanopores and to perform single-molecule DNA detection. Then I will review the physical design of the custom instrument combining single-molecule fluorescence and electrical detection: I will initially describe the home-built components and then will briefly review the commercial components of the instrument. Finally I will show how the electrical and optical system are integrated and performed simultaneously.

2.1 Review of the Electrical instrumentation of a nanopore system

A standard nanopore setup comprises all the equipment necessary to detect single molecules translocating through a nanopore. At each side of the nanopore there is a fluidic reservoir of electrolyte solution, built in a polytetrafluoroethylene (PTFE) fluidic cell. The cell provides the mechanical structure to make a seal around the nanopore, in such a way that the nanopore is the only fluidic path between the two reservoirs: a nanopore chip is squeezed between two circular silicone elastomer gaskets with an aperture in the centre to make a gigaohm range seal. In each reservoir an Ag/AgCl electrode is placed. Upon application of an electrical potential difference between two electrodes, ions move through the nanopore and at the electrode interface the following reversible reaction takes place:

$$\mathrm{Ag} + \mathrm{Cl}^- \leftrightharpoons AgCl + \mathrm{e}^-$$

to transform ionic current in the nanopore into an electronic current. The electrodes are connected to a commercial patch clamp current amplifier such as the Axopatch 200B or Axopatch 700B (Molecular Devices). The current measurements in solid-state nanopores are usually done in a resistive feedback mode, since currents are in the range of 1-100nA, depending on the nanopore size and electrolyte conductivity. The current signal, once amplified and converted into a voltage by the Axopatch, is digitized and recorded by a computer controlled data

acquisition card (DAQ card) with the help of a custom LabView program. The Axopatch amplifier has a separate channel to send the current signal to an oscilloscope for real time visualization of the current trace. During electrical measurements, the nanopore is enclosed by two Faraday cages to minimize EM pickup noise. For a more detailed discussion on standard nanopore experiments instrumentation, see Chapter 3 of the book Engineered Nanopores for Bioanalytical Applications [24].

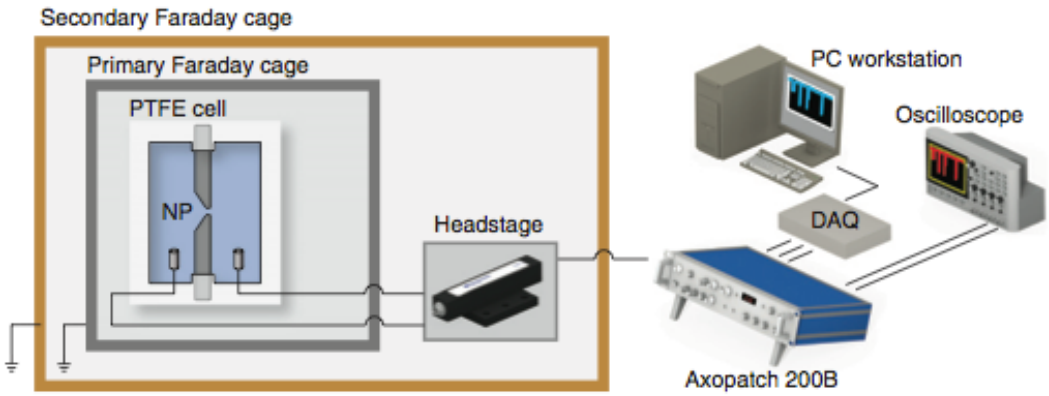

Figure 2.1 Schematic diagram of a nanopore recording setup. Reproduced with permission from reference[24].

2.2 Physical design of the nanopore based optofluidic instrument

A schematic diagram of the whole instrument is shown in Figure 2.2. The nanopore is at the centre of the aluminium holder and of the custom built Faraday Cage. A PDMS cell is constructed around the chip to separate the two fluidic reservoirs.

The headstage (first amplifier stage) of the Axopatch is connected to two electrodes on each side of the dielectric membrane. The PDMS cell is positioned on top of the inverted microscope for optical imaging. I will now describe the individual components of this nanopore based optofluidic instrument.

2.2.1 Transmission Electron Microscope (TEM) windows as support membranes for nanopores

Solid-state nanopores are fabricated in a thin free-standing membrane such as silicon nitride TEM windows, shown in Figure 2.3. These membranes were originally fabricated to image samples under TEM. The free-standing membrane where the nanopore will be drilled is fabricated in the following way: a thin layer of silicon-rich, silicon nitride is deposited on a silicon wafer (usually 200 μm thick) by low-pressure chemical vapour deposition (LPCVD). This creates a low-stress silicon nitride SiN_x, which is a good insulator and a mechanically robust material. Other materials like silicon dioxide, or hafnium oxide can also be used. The thickness of the film can be controlled with sub-nanometer precision. Thinner films are preferred because they increase the sensitivity to single molecule events, but the membranes become fragile. A good compromise between adequate robustness and high sensitivity is accomplished with 10-nm or 30-nm thick SiN_x membranes, which are available commercially. For my work, I used membranes from Norcada Inc., product # NT005X and NT005Z.

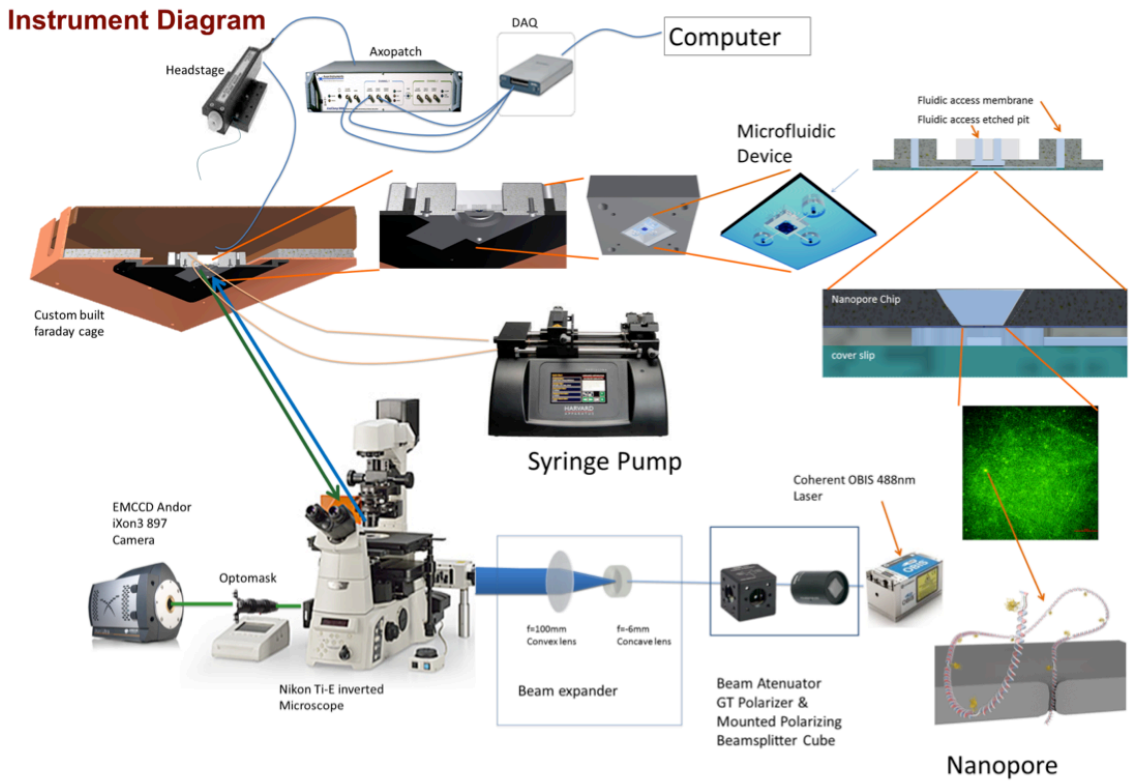

Figure 2.2 Schematic Diagram of the entire instrument. In addition to the electrical system, the instrument has an optical fluorescence system. A 488nm laser beam is expanded and fed into the microscope to serve as the illumination source. Stained- DNA absorbs light at 488nm and emits light at 510nm. That light is filtered and collected by the EMCCD iXon camera, which has the capability to detect a single photon. The flow of solution with DNA is stabilized using a syringe pump.

Once the SiN_x film has been deposited, both sides of the wafer are coated with photoresist, which is then developed to make a square opening on one side of the wafer. Reactive Ion Etching (RIE) is then used to remove the SiN_x that has been exposed. The result is that the silicon wafer is exposed at this particular location. The silicon is then etched away using the SiN_x as a mask in a solution of KOH. The etching is anisotropic and a particular angle is created, so that the window that

was made is scaled down in a pyramidal shape until the other end of the wafer is reached. The SiN_x, on the opposite side of the wafer, acts as an etch stop and forms a free-standing membrane in which a nanopore can be fabricated. A detailed discussion of this process can be found in reference [10] . The wafer is cut into 3mm diameter chips with a single 50x50 μm^2 SiN_x membrane in their center. The chips that were used for this work were purchased from Norcada.

A schematic model of the chip is shown on Figure 2.3.

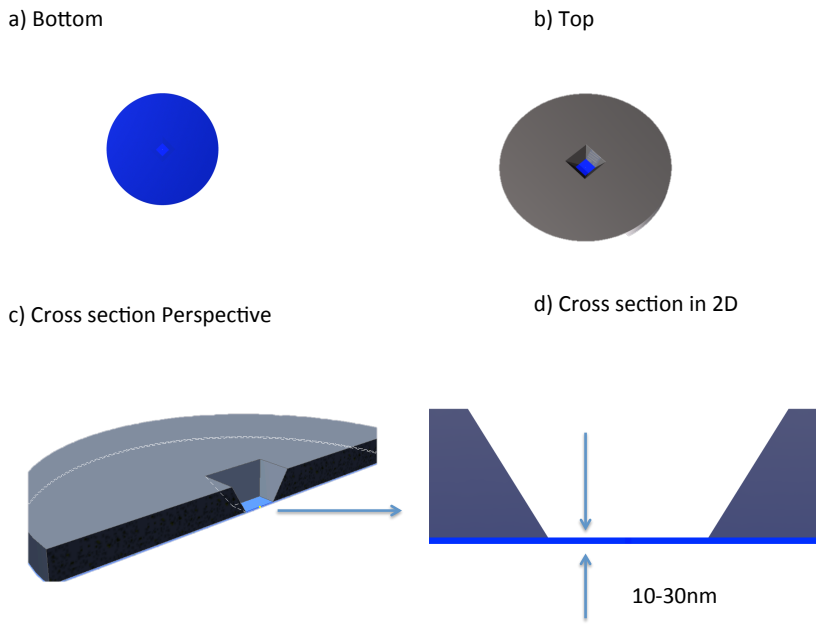

Figure 2.3 Schematic representation of the nanopore chip. Using the process described above, the silicon on the window is etched away, and a SiN_x free-standing membrane is created with a supporting structure.

2.2.2 Optical Constraints

The optical measurements that the system will be able to make are limited by the performance of its elements. The objective in use is a critical part of the optical

magnification setup. It will determine the resolution, the volume that will be imaged, the brightness and the space available for the system to be implemented in. We will express these quantities in terms of the numerical aperture N.A. defined as[25, 26]:

$$N.A. = n\ sin\theta \tag{2.1}$$

where n is the refractive index of the medium (n=1.33 for water) and θ is half of the angle of collection of light of the objective. I used a N.A.=1.27 water objective, which implies an angle at which light will be collected is 144°.

The numerical aperture defines the three important parameters of an optical setup, such as the resolving power:

$$R = \frac{0.61\lambda}{N.A.} \tag{2.2}$$

which is the distance at which two dots should be placed for the instrument to resolve them as different objects. With a wavelength of 488nm the instrument has a resolving power of 234 nm.

The depth of focus DOF is the thickness of the optical section along the axis of the objective within which the objects in the sample are in focus. It defines a thickness of detection, all the objects in that range will be portrayed in the image. The depth of focus is defined as

$$\text{DOF} = \frac{\lambda}{N.A.^2} \tag{2.3}$$

In this case the DOF is 302nm. To put this figure in perspective, I will detect a depth ten times thicker than the silicon nitride membrane. The brightness of the image is also proportional to the Numerical aperture over the total magnification (Brightness $\propto$ (N.A. / total magnification)^2.

Finally, the working distance of the objective is the distance between the top lens of the objective and the cover glass when the sample is in focus. In our case the working distance is 170 μm. It constitutes a big obstacle for the development of the instrument, since the nanopore needs to have a fluidic reservoir in front of it. This reservoir shall then be no thicker than 170 μm.

2.2.3 Microfluidic Device

The working distance of the high numerical aperture microscope objective (Nikon Plan Apo IR 60X, NA=1.27) is 170 μm. This imposes the restriction that the sample (Silicon nitride membrane) needs to be placed no further that this distance from the objective for a focused optical image to be formed. A solution, to not only provide optical access but also fluidic and electrical access to the membrane side of the chip, was to create PDMS microfluidic channels mounted on a cover slip. These channels were designed to be thin enough to position the SiN_x membrane within the working distance of the objective, and allow the electrolyte solution to be flowed to the nanopore, providing fluidic and electrical access.

I manufactured the channels using photo lithography.[27] A protruding pattern, that serves as a mould for the fluidic channels, is created on a silicon wafer: a layer of SU-8 2050 photoresist is spin coated on the wafer. The thickness of the spin-coated layer can be controlled with the angular velocity of rotation and the duration. I aimed for a thickness of 50 μm (two step process: 500 rpm for 10s, 133 rpm/s, 3000 rpm for 30 s 266 rpm/s). Then, selected regions of the photoresist are exposed to UV light, using a mask. The UV light fixes the photoresist that has been exposed, but all the unexposed photoresist can be removed by immersing the wafer in SU8 developer. In this case, the remaining protruding features are the channels.

After the master wafer has been created, Poly(dimethylsiloxane) (PDMS), is spin coated on the wafer. The thickness of the resulting layer is tuneable. We select 100 μm. The PDMS is then cured in an oven at 80 °C for two hours. A 100 μm PDMS layer is produced with intruded features 50 μm deep, as seen in Figure 2.4e

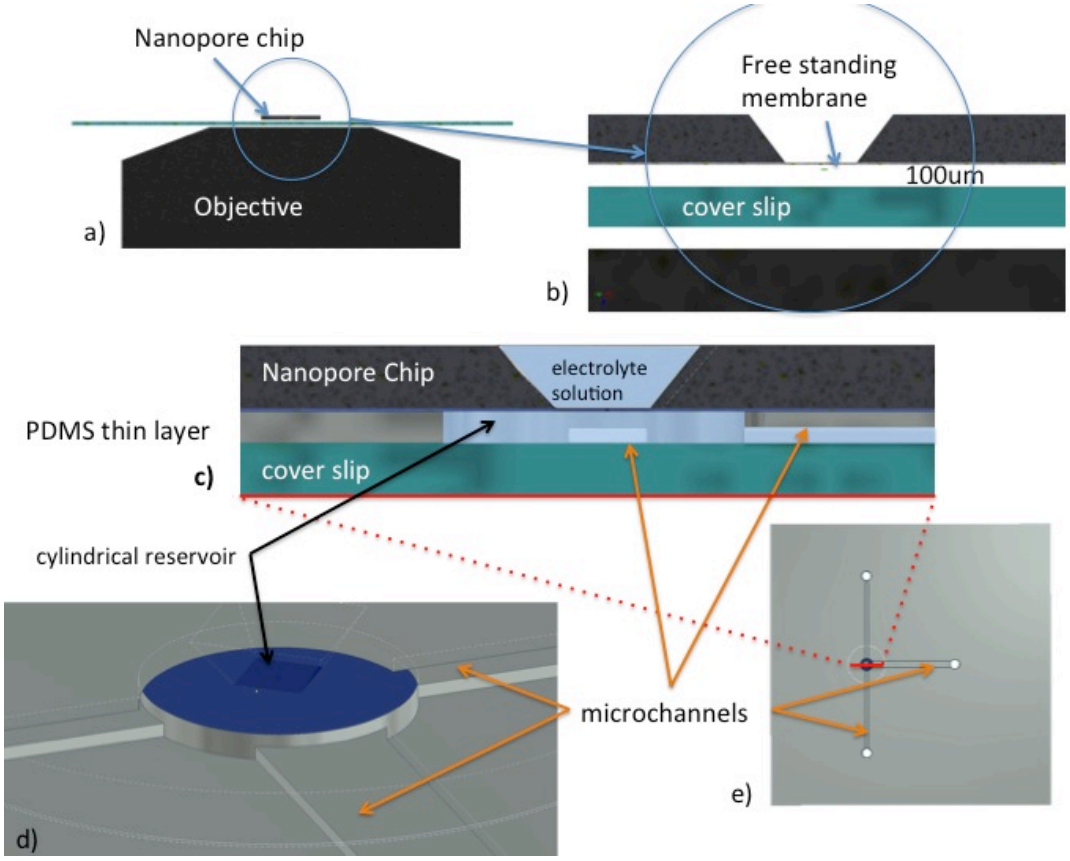

Figure 2.4 Microchannels design. The device construction is constraint by the working distance of the microscope objective, which is 180um from the cover slip. a) Illustration to scale of the size of the objective, the nanopore chip and the cover slip. b) Zoom that shows the room we have to work between the sample (nanopore chip) and the cover slip. c) PDMS microchannels were placed between the cover slip and the chip to allow fluidic access to the membrane. The image is a cross section of inset e), where the whole thin PDMS film with the embedded channels is shown. d) 3D view of the channels as they meet below the chip. A cylindrical reservoir is formed below the membrane. (cover slip has been removed) e) PDMS thin film, the film is 100 μm high and the channels protrude 50 μm into it. It has the same dimensions as the cover slip.

At the bottom of the thin PDMS layer the glass cover slip is bonded by treating both surfaces in an oxygen plasma oven (60s, 60W). The cover slip closes the channels and forms the bottom layer of the flow cell assembly. PDMS binds very well to glass, so the cover slip makes a thigh seal and prevents solution from leaking. At

the top of the PDMS thin layer the nanopore chip is bonded (with the membrane facing the objective), also with oxygen plasma. This bond creates a tight seal so that there is no fluidic connection between the two sides of the chip except through the nanopore.

For structural purposes, a thicker PDMS piece (we will refer to it as PDMS mould) is bonded on top of the thin membrane as in Figure 2.5b. This piece is shaped with an custom-machined Aluminum mould to have certain particular characteristics, namely: provide a fluidic seal to the tubes that will flow the fluid to the microchannels, serve as part of the fluidic reservoir on the etched pit side of the nanopore chip, and finally, provide structural support to the thin PDMS membrane so that it can be handled with ease and fitted in a holder on top of the inverted microscope. The thick PDMS piece is fabricated using 5:1 (5 parts elastomer: 1 part curing agent) PDMS, because it bonds well to the 10:1 thin PDMS film described in Figure 2.4. It has a circular opening to accommodate the nanopore chip.

On top of this square opening where the chip is housed, a slab of PDMS is bonded over the PDMS mould to make the fluidic reservoir of the etched pit side (Figure 2.5c). Two holes are punched into this slab to make an inlet and an outlet, with a TED Pella 0.75 mm hole puncher. Three more holes are also punched in the cylindrical columns of the PDMS mould, for tubes to be inserted in them and fluid to flow in the bottom channels (Figure 2.4).

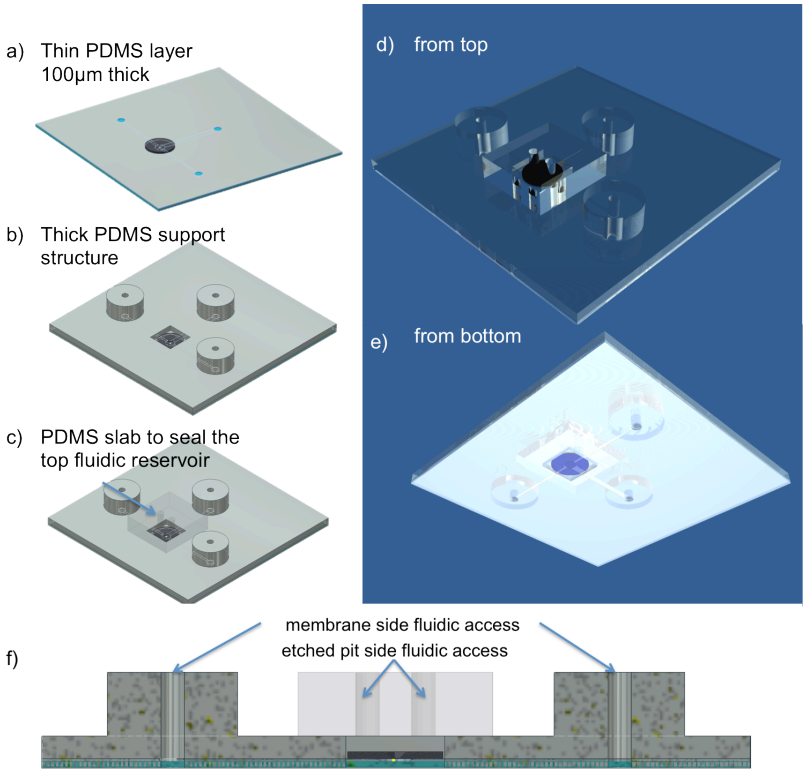

Figure 2.5 Microfluidic device. This PDMS based fluidic device allows us to bring the sample (nanopore) to the working distance of the objective (180um over the cover slip). We can see how the last part of the device is assembled: a) the nanopore chip is bonded over the thin PDMS film, and this film is bonded over the cover slip. b) A thick PDMS mould is placed over the thin PDMS film. c) A thick PDMS slab is bonded over the PDMS mould to close the fluidic reservoir on top of the chip. e) Image of the finished microfluidic device as seen from the top d) image of the microfluidic device as seen from the bottom. Notice how the 3 microfluidic channels are visible.

Three access channels to the membrane side are used as opposed to just an inlet and an outlet. The design also features a separate wider access channel for the electrode to help reduce access resistance. The redundancy has proven to be useful in the case of fabrication errors in one of the channels, and to improve the mixing possibilities inside the channels (in this low Reynolds number regime mixing is not

trivial). Nevertheless only two channels are strictly necessary since the electrode channel can also serve as an inlet or outlet.

2.2.4 Mechanical Positioning of the Microfluidic Device

To position the microfluidic device on top of the microscope I have built several holders. The first aluminium holder has the purpose of holding the device, which is clamped between the holder and an aluminium plate (Figure 2.6b). This holder also has cylindrical intrusions to hold the vials of the fluidic reservoirs close to the microfluidic device. (Figure 2.6d). The first holder is placed on top of a XY motion stage (H117P2NN, Prior) with a step size of 0.01μm. In Figure 2.6c, I have drawn schematically the interface of the XY stage only with the holder.

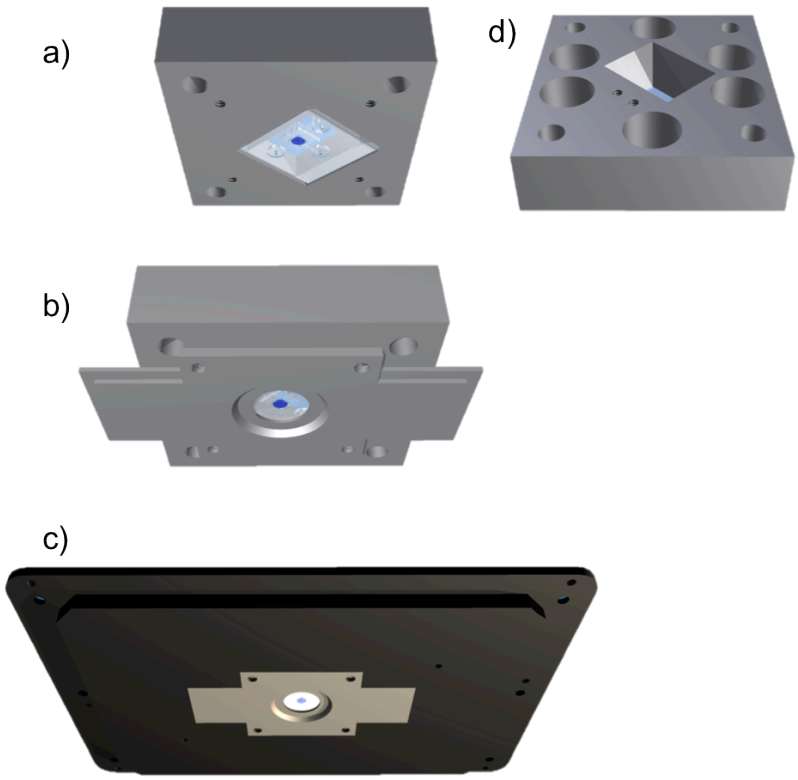

Figure 2.6 Holders for the microfluidic device. a) The first holder positions the microfluidic device on top of the microscope, and also holds the liquid vials. b) An aluminium plate is used to secure the device in place. c) The holder with the securing place is inserted on a holder from the XY stage (shown in black).

2.2.5 Faraday Cage

To protect the setup from external noise, I have enclosed it in a Faraday cage. The Faraday cage cannot be complete since there needs to be an optical access for the microscope, however this is the only opening of the Faraday cage. Note, that an Indium Tin Oxide (ITO) coated-glass cover slip could also be employed to realize a full shield, but this was not implemented at this stage because of cost considerations. The electrical noise consequences of this opening are discussed in

Chapter 3. The Faraday cage is built of copper sheet and then folded to accomplish the desired shape. (Figure 2.7) Inside the Faraday cage we can see the Axopatch headstage (remote current amplifier is positioned as close as possible to the sensing electrode to reduce noise pick up) used to perform electrical detection of single DNA molecules. There is also the fabrication circuit that is used for nanopore fabrication by controlled dielectric breakdown[11]. I have fabricated a support plate that serves multiple purposes, it holds the headstage in place and it provides support for tubing coming from the syringe pump (see section Flow Control on page 51). To minimize acoustic noise we secure all the elements inside the Faraday cage to this plate.

Traditionally two Faraday cages are used, one that encloses just the fluidic cell very closely, and another that encloses all the setup as seen in Figure 2.1. I have found that it is best to use one Faraday cage that encloses the fluidic device and the headstage, and another that enclose the whole instrument, including the microscope, camera, and laser.

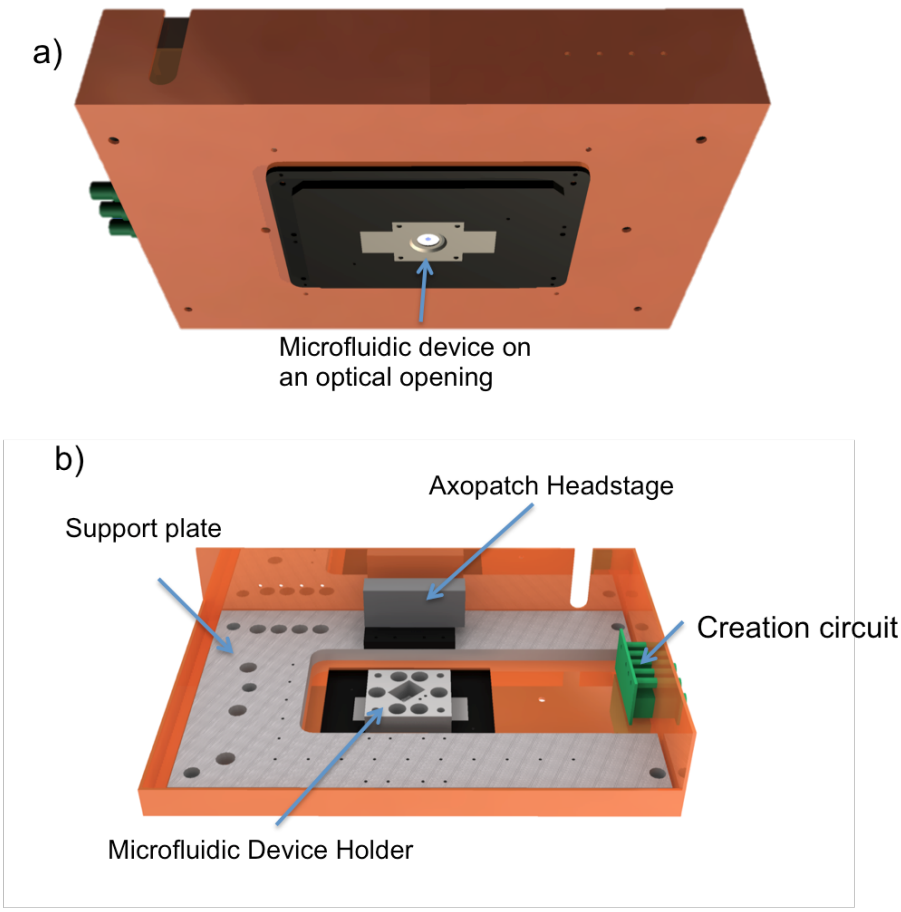

Figure 2.7 Faraday Cage design. a) Bottom view of the Faraday cage illustrating the optical access for the microscope, which makes the cage incomplete. Electrical noise consequences are discussed in Chapter 3. b) Top view of the opened Faraday cage. One can see the placement of the elements inside the cage. The headstage of the Axopatch is used for electrical detection of single DNA molecules, and the nanopore fabrication circuit is used for the creation of nanopores via dielectric breakdown. c) View of the closed Faraday Cage.

2.2.6 Flow control.

I have found that it is very important to control precisely the flow into the microfluidic cell. An excessively high flow can cause the nanopore to enlarge and, when the flow is not stopped properly during a DNA experiment, optical detection is difficult due to the fast motion of the molecules.

A syringe pump is usually the choice to have a precise control of the flow down to nL/s. However fluidic tubes, filled with liquid electrolyte, cannot run from the device to the syringe pump since they act as antennas and pick up a lot of noise. (See chapter 3) To prevent this inconvenience I have designed a set of vials that interface air with electrolyte solution as seen in Figure 2.8. I connect a tube filled with air from the syringe pump to the vials, and then liquid of the vials feels the pressure change and starts flowing through the tubes connected to the microfluidic device. This way the flow of liquids inside the cell, enclosed in the Faraday cage, can be controlled without conductive tubing exiting the Faraday cage. A schematic diagram of this strategy is shown in Figure 2.8

This strategy has proven to be very successful. In the direction of the flow, the average position of a diffusing single molecule can be controlled within a couple of micro meters, so that capture can be induced by bringing the molecule to the capture radius of the pore (typically a few microns).

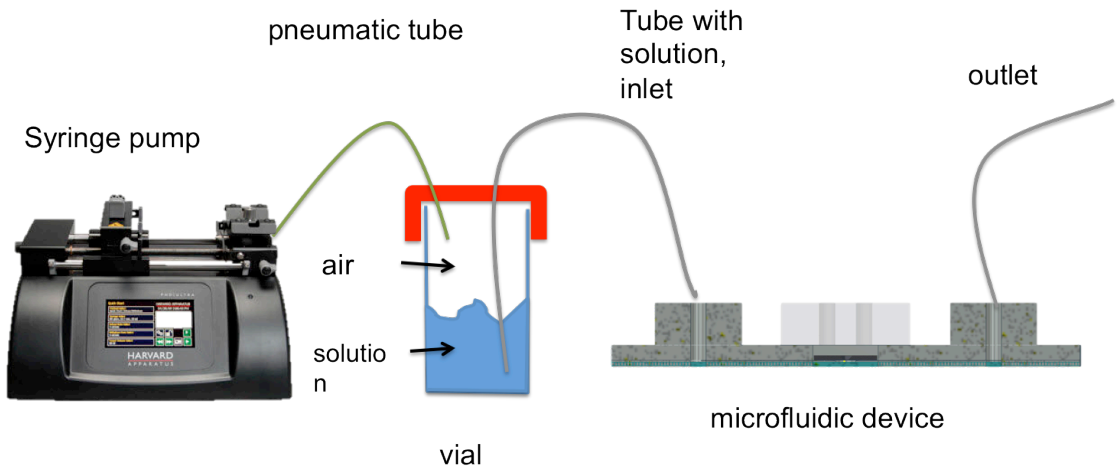

Figure 2.8 Flow control. It is accomplished with a syringe pump that injects air into a vial, electrolyte solution reacts to pressure and is injected in turn to the microfluidic device. This flow control has proven to be very effective. The position of the molecules can be controlled to a couple of micrometers in the direction of the flow.

2.2.7 Laser beam expander

To excite the fluorescently labelled DNA molecules, we use a 488 nm laser diode (Coherent OBIS 488nm). To illuminate a wide field, we expand the collimated beam size from d = 0.7-mm up to d = 12-mm. I accomplish this with two lenses. The first lens is a Bi-Concave lens with a focal distance of f = -6-mm (N-SF11, Thorlabs) which expands the beam. The rays become parallel again with a Bi-convex lens with a focal distance of f = 100-mm (N-BK7, Thorlabs). The two lenses are separated with a distance of (100-6) mm = 94-mm. A schematic diagram of the beam expander is shown in Figure 2.2.

2.2.8 Optical attenuator

An optical ability to control the intensity of the illumination was necessary to accommodate the optimal illumination of the Stained DNA when using the laser at its designed power. An attenuator was then designed using Glan-Thompson polarizer (GTH10M, Thorlabs) with a high extinction ratio (1:10000). The polarization was then rotated with a Half Wave plate (WPH10M-488), and passed through a second polarizing beam splitter cube (CM05-PBS201, Thorlabs). The attenuation will be given by Malus law[26]

$$I = I_0 cos^2(\theta) \tag{2.4}$$

where I is the resulting intensity, I_0 is the initial intensity, and θ is the angle between the second polarizer and the direction of polarization of the incident light.

2.3 Description of the commercial components of the instrument

The rest of the instrument is made of commercially available elements such as the Nikon Ti-E inverted microscope. These elements will be described and discussed.

2.3.1 Microscope

The microscope I used is the Eclipse TI-E (Nikon). It is a motorized inverted microscope with both transmitted and reflected imaging capabilities, and includes an automatic focusing system (a.k.a perfect focus system, PFS). It is completely controllable from the computer.

The perfect focus system is a capability in which the microscope maintains focus of a plane in the sample automatically. The mechanism to do this is an infrared LED that illuminates the sample to measure the sample height with respect to the microscope objective in real time and adjusts it accordingly. The measurement is done by adjusting the position of a reflected ray of light into a line-CCD sensor (http://www.microscopyu.com/tutorials/flash/focusdrift/perfectfocus/).

Unfortunately, in my particular application, all the electronic capabilities of the microscope cannot be used. First, the LED illuminates the sample and causes additional noise on the ionic current signal through the nanopore. Sadly, the microscope does not have a way to simply turn this LED off, the only way to switch it off, is by disconnecting the module that contains, among other capabilities, the PFS.

Furthermore, the motorized microscope adds noise to the system (See chapter 3). The only way to suppress this noise is to position the microscope in the desired configuration (sample focused, filter cube and imaging ports set, etc.), and switch the whole microscope off. The electrical noise produced by the microscope is suppressed, but the configuration of the microscope cannot be easily changed, since it resets itself once it is turned on again.

http://www.nikoninstruments.com/Products/Microscope-Systems/Inverted-Microscopes/Eclipse-Ti/%28key_features%29

2.3.2 Camera Andor iXon3 (897)

This camera is a state of the art back illuminated Electron Multiplying Charge Coupled Device (EMCCD). It has single photon capabilities combined with quantum efficiency larger than 90%. The sensor has 512x512 pixels, 16 μm in size, and its maximum frame rate at full resolution is 35fps. However, it can be operated with cropped sensor mode to 512x1 pixels (or any other pixel combination) and reach speeds of 7,980 fps. With a 60X 1.27NA water immersion objective a single pixel represents ~200nm of field of view. Considering the radius of gyration of a DNA molecule, such as λ DNA (48.5kbp) is <1μm, this pixel size is sufficient for my applications (*e.g.* tracking DNA translocation through a nanopore).

The camera can image DNA molecules at the single molecule level (see Chapter 4 for results). The quantum yield (photons emitted/photons absorbed) of YOYO-1 dye is 0.38[28] and since the DNA is stained with one YOYO-1 molecule per 10bp, the amount of light is sufficient to detect DNA reliably. The cameras sensitivity allows us to easily monitor the motion of single DNA molecules in real time and study the interaction of the nanopore and the DNA.

The camera also provides tools to synchronize the optical signal with the electrical signals of voltage and current. It has several operating modes. I have found the

most useful one to set the camera to wait for a digital pulse to start acquiring. This pulse is readily sent from the DAQ card when the electrical acquisition has started. Once the camera receives this pulse, it starts acquiring with the parameters that have been set on the computer. I used the software NI-Elements to drive the camera. When the camera is acquiring video, it produces a signal (trigger), which indicates precisely when it is exposing (trigger=1V) and when it is not, (Trigger=0V). This signal is recorded by the DAQ card, which allows synchronization between the optical and the electrical signals. A custom LabView program was written to accomplish this task.

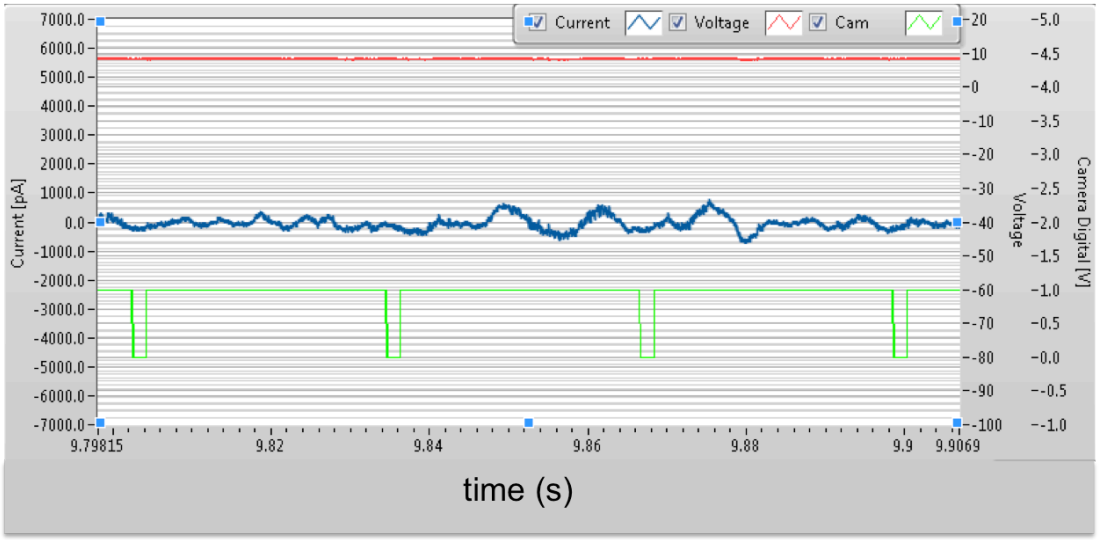

Figure 2.9 Synchronized current, voltage and camera signals. Sample diagram of the current signal (blue), the voltage applied to the membrane (red), and the camera signal (green), when the camera signal is high (at 1V) the camera is exposing, and when it is low (0V) it is not exposing.

More information about the camera we use can be found in the following link:

http://www.andor.com/scientific-cameras/ixon-emccd-camera-series/ixon3-897

2.3.3 Coherent OBIS 488-nm Laser Diode

We chose this laser to excite fluorescein-based dyes (YOYO-1, SYBR-green, ALEXA-fluor dUTPs), which range from 488 to 490 nm. It also has a good power stability (<0.25% according to manufacturer) at full power and has a circular beam profile (beam diameter = 0.7mm) for a uniform illumination.

This particular laser diode has an intensity that can be controlled from the computer. It ranges from 0.1mW to 50mW. However, the rms noise (stability) is not constant over the whole power range. Actually, at low powers it has significant low frequency noise. The laser stability is best when operated at 50mW.

The complete specifications of the laser diode can be found in the following link:

http://www.coherent.com/download/8093/OBIS-and-OBIS-FP-Family-Data-Sheet.pdf

2.3.4 Prior H117P2NN Stage with ProScan III Controller.

The stage used is specifically designed for an inverted Nikon Ti-E Microscope. It has a minimum step size of 0.01-µm according to the vendor.

http://www.prior.com/downloadcentre/documents/brochuresanddatasheets/H117%20Datasheet.pdf

2.3.5 Axopatch

For the experiments I used two different commercial current amplifiers. Most of my work was done with a MultiClamp™ 700B amplifier (Molecular devices), which is a microelectrode amplifier for ionic channel recordings. It supports up to 4 headstages and as a computer-controlled interface with many automated features. It has a maximum bandwidth of 30kHz with pA current resolution. I also used a Axopatch 200B amplifier (Molecular devices), which only has one headstage, but allows for maximum bandwidth of 100kHz with pA current resolution. When I compared the model 700B with the 200B I found that the Axopatch 200B was superior in terms of noise performance.

Detailed information about the Axopatches can be found in the following links:

200B: http://www.moleculardevices.com/Products/Instruments/Axon-Patch-Clamp/Axon-Axopatch.html

700B: http://www.moleculardevices.com/Products/Instruments/Axon-Patch-Clamp/Axon-MultiClamp.html

2.3.6 Syringe Pump PHD Ultra Syringe Pump 703009

The syringe Pump was purchased from Harvard Apparatus. Its main purpose is to be able to infuse liquid in a controlled, gentle manner. It is also used to control the flow of solution to clearly see DNA molecules and to not prevent their translocation. It has a minimum infuse /withdrawal rate of 1.56pL/min.

More information can be found here.

http://www.instechlabs.com/Support/manuals/703005_PHD_ULTRA_Manual.pdf

2.3.7 External Faraday Cage

The external Faraday Cage is a box made with a metallic mesh. It encloses the whole instrument and it is connected to the metallic floor of the optical table where the microscope is installed.

3 Electrical Noise Analysis and Minimization in Nanopore based Optofluidic Systems

In order to characterize and discuss the noise encountered in a nanopore based optofluidic system, I will first introduce the general theory of electrical noise in nanopores without any optics. I will write a brief description of the types of noise and their sources that have been reported in the literature[24,29,30], and will then show how each type of noise changes with the integration of fluorescence microscopy. I will focus on the types of noise that more significantly distort the nanopore electrical signal. Finally I will report methods of noise minimization that I have succeeded in implementing on the custom built instrument that I report here. This analytical and practical work should prove useful for the future

development of similar instruments aiming to combine high-resolution fluorescence microscopy and low-noise, high bandwidth electrical detection through nanopores.

3.1 Signal-to-noise ratio when detecting individual DNA molecules electrically

The electrical signature of a DNA molecule translocating from one side of the membrane to the other can be represented as a change in conductance of the nanopore using equation 1.2 [19]:

$$\Delta G = -\frac{1}{L_{pore}}\left(\pi r_{\mathrm{DNA}}^2(\mu_K + \mu_{Cl})n_{KCl}e - \mu_K^* q_{l,DNA}^*\right) \tag{3.1}$$

Where ΔG is the change in conductance in the pore, L_{pore} is the length of the pore, r_{DNA} is the radius of DNA, μ_K and μ_{Cl} are the electrophoretic motilities of potassium and chlorine ions respectively, $q^*_{l,DNA}$ is the effective charge of the DNA per unit of length, μ^*_K is the effective electrophoretic mobility of the potassium ions along the DNA, n_{KCl} is the number density of potassium or chlorine ions and e is the elementary charge. The values reported by Ralph et al.[19] can be used to estimate the change in conductance. They reported

Table 3.1 Parameters to calculate the Conductance change upon translocation of a DNA molecule on a nanopore.	
Parameter	Value
μ_k	7.616×10^{-8} m^2/Vs
μ_{Cl}	7.909×10^{-8} m^2/Vs
d_{DNA}	2.2 nm
$\mu_K^* q_{l,DNA}^*$	$2.09 \pm 0.06 \times 10^{-17}$ m/Ω
n_{KCl}	2.17×10^{27} m^{-3} (assuming 3.6M)
E	1.60×10^{-19} C

Using these values we obtain ΔG =-6.1 nS for L_{pore} = 30nm. Assuming a voltage of 200mV we will have a change in current ΔI = -1.22 nA.

The values obtained experimentally usually range from 1nA to 100pA. (The variation is due to changes in concentration of the solution, geometry of the pore , thickness of the membrane). To detect DNA efficiently, the current blockage must be greater than the peak-to-peak noise. Using Gaussian statistics $I_{pp} \sim 8 I_{rms}$, therefore the blockage $|\Delta I| > 8\ I_{rms}$. A SNR= $|\Delta I| / I_{rms} \geq 8$ is necessary. Therefore, the maximum electrical RMS current should be 125pA in the best scenario and 12.5pA in the worst.

Our instrument is limited by additional constraints. A common way to study DNA fluorescently is to attach intercalating dyes into double stranded DNA (dsDNA)

such as YOYO-1. This fluorescein-based molecule is excited at 490nm and emits light at 510 nm, and is very convenient to make purely optical measurements. However, it has a major disadvantage, it needs a concentration of electrolyte lower than 150mM to stay bound to the DNA. At higher concentration the charge of DNA is screened by the electrolyte and the fluorescent molecule does not interact with the DNA.

When the values for 100mM electrolyte concentration are substituted into equation (3.1) the current change when a DNA molecule enters the pore is quite different, instead of observing blockages, one sees increases in the current. The actual calculated current change using the parameters used before is ΔI= +0.3 nA. Then the maximal noise level should be of 37.5 pA. This noise cap, in addition to all the extra sources of electrical noise, makes noise optimization a paramount aspect of this instruments design.

3.2 Quantification of Electrical Noise

The noise content of a signal is measured with a Power Spectral Density (PSD) function. Given a signal in time $x(t)$, its Fourier transform evaluated on the interval $[0,T]$ is

$$X(T,f) = \frac{1}{T}\int_0^T x(\mathrm{t})\, e^{-i2\pi f t} dt \tag{3.4}$$

The PSD of the signal $x(t)$ is defined as [31]

$$S(T,f) = \frac{|X(T,f)|^2}{T} \tag{3.5}$$

$S(T,f)$ represents the power density as a function of frequency, so that the spectral components of the noise can be observed. Sometimes the interval where the time trace was taken is ignored and we refer to $S(T,f)$ as $S(f)$.

One can relate the PSD of a time series $x(t)$ to its power through the equation

$$\bar{P} = \int_{-\infty}^{\infty} S(T,f)df \tag{3.6}$$

Since the mean power of a signal $x(t)$ on an interval $[0,T]$ is defined as

$$\bar{P} = \int_{0}^{T} |x(t)|^2 dt \tag{3.7}$$

and the signal x(t) in our case is an electric current, one can readily relate the PSD of the current to the root mean square current I_{rms}

$$\bar{P} = \int_{-\infty}^{\infty} S(T,f)df = {I_{rms}}^2 \tag{3.8}$$

where I_{rms} is defined as,

$$I_{rms} \equiv \sqrt{\frac{1}{T_2-T_1}\int_{T_1}^{T_2}[I(t)]^2 dt} \tag{3.9}$$

In the figures we used to characterize the noise in our system, we will show the PSD S(T,f) and the rms current, which can be calculated by simply taking the square root of the integral P.

A low pass filter is usually utilized to reduce high frequency noise. In that case, the rms current can be calculated as[24] :

$${I_{rms}}^2 \cong \int_{0}^{f_c} S(T,f)df \tag{3.10}$$

Where f_c is the cutoff frequency of the lowpass filter. In this chapter I used analogue four pole 100kHz Bessel filter unless otherwise indicated.

3.3 Electrical Noise in a Nanopore System

A schematic of a PSD of the ionic current of a nanopore system can be seen in Figure 3.1. The PSD is given by the polynomial equation [3.2]

$$S(f) = \frac{a_0}{f} + a_1 + a_2 f + a_3 f^2 \ \ [A^2 s] \tag{3.11}$$

Each term of equation 3.11 is related to a different mechanism of noise generation. The coefficients a_0, a_1, a_2, a_3, represent the weight of the contribution of the following types of noise, Flicker (pink), Thermal (white), Dielectric (blue), and Capacitive (purple), respectively. Each one of these noise types is produced by a different mechanism and dominates in a different range of the frequency spectrum. In addition to these inherent noise types there is always external electrical noise that is picked up by the system and incorporated into the signal. I will refer to this noise as Pickup Noise.

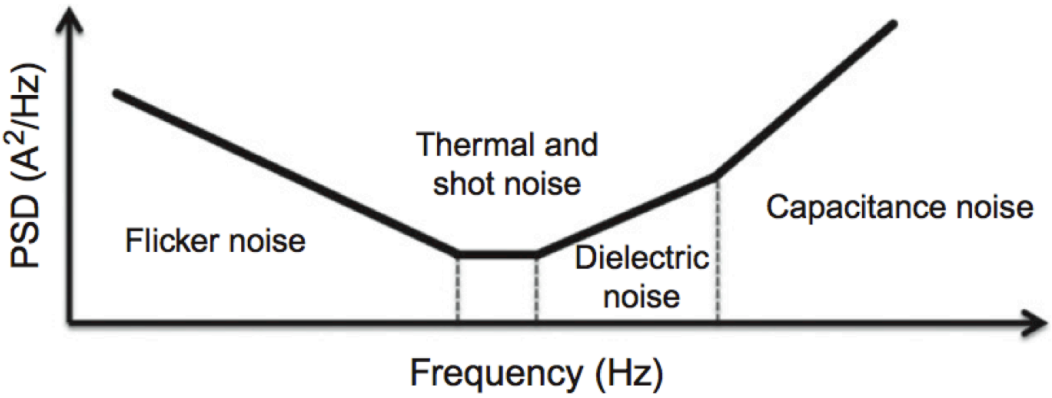

Figure 3.1 Dominant Sources of noise in a nanopore setup. Schematic representation of the dominant sources of noise in a PSD of the ionic current of a solid-state nanopore as a function of frequency. The PSD is given by equation 3.11. Reproduced with permission from [24].

In the case of nanopore-based single-molecule electrical detection combined with fluorescence microscopy there are additional or amplified noise sources related to the illumination of the sample (the membrane, the nanopore and the supporting chip) during the experiments. I will treat this noise as Illumination noise.

3.3.1 Flicker Noise

Applying an electric potential across a membrane with a nanopore gives rise to a low frequency fluctuation of the ionic current flowing through the pore, called flicker, $1/f$ or pink noise. This behaviour is present in a variety of systems and has been extensively studied[2,30,32–35]. However it has not been successfully explained.

The flicker noise largely dominates the low frequency spectrum, surpassing thermal and shot noise <100Hz or <1kHz when this noise type is high. It has been

hypothesized that flicker noise is produced by either (i) nanobubbles inside the pore channel or partially wetted pores[36,24] , (ii) variations in the surface charge of the nanopore channel walls[30]. This type of noise can be modeled as

$$S_{\text{Flicker}} = \frac{\alpha I^2}{N_c f^{\beta}} \tag{3.12}$$

Where I is the average ionic current though the nanopore, N_c is the number of charge carriers, α is the Hooge parameter that quantifies the flicker noise and the exponent β is typically unity[24] . All these parameters can be combined into one single coefficient a_0.

Flicker noise has a significant variability from one nanopore to another. To minimize flicker noise, we fully degas all solutions used: we use a vacuum chamber immersed in a sonicator and leave the solution there until bubbles stop forming into the liquid (15-20 minutes). We also treat the membrane surface with Oxygen Plasma at 60W for 30s to clean it and increase its hydrophilicity. Using this protocol, the amount of flicker noise observed in our optofluidic system is comparable to the flicker noise level in standard nanopore experiments with no optics.

3.3.2 Thermal Noise

Thermal noise is the fluctuation of the charge carriers due to their Brownian motion while they are in the conducting medium. It is present on a nanopore system in two main forms: 1) there is thermal noise originating from the resistance

of the pore in the solution due to the random motion of ions in the nanopore, which sets a minimum noise limit on the system. 2) There is also a contribution of thermal noise from the electronic amplifiers, mainly on the feedback resistor of the current amplifier circuit of the headstage of the Axopatch.

Thermal current noise is frequency independent (hence denoted as white noise) and its PSD is simply

$$S_{Thermal} = \frac{4k_BT}{R} \tag{3.13}$$

where $4k_BT = 1.6 \cdot 10^{-20}\, J$ and R is the resistance of the nanopore or the feedback resistance of the amplifier.

In reality all the thermal noise contributions add up, and should be summed as

$$S_{thermal} = 4k_BT\left[\frac{1}{R_{pore}+R_{feedback}+R_{access}}\right] \tag{3.14}$$

However, the contribution of only the largest resistance (generally the pore) dominates and the rest are ignored.

The thermal I_{rms} can be calculated readily from this noise PSD:

$$I_{rms} = \left\{\int_0^B S_{Thermal}\,df\right\}^{1/2} = \sqrt{\frac{4k_BBT}{R}} \tag{3.15}$$

where B is the integration bandwidth in Hz.

As an example, we can calculate the thermal noise of a nanopore in one of the devices that we will use later for noise characterization (device B10.7). The nanopore had a conductance G = 22.8 nS, that is R =43.8 MΩ. Then $S_{Thermal} =$

3.78 $x10^{-4} pA/Hz$ which yields I_{rms} = 1.94pA assuming a bandwidth of 10 kHz, and I_{rms} = 6.14pA for B=100 kHz.

3.3.3 Dielectric Noise

Dielectric materials are not perfect insulators. Some current leaks through when an electric field is applied across them (i.e. they do not store charge perfectly) and the membrane acts as a capacitor in parallel with a resistor. We define then an Equivalent Series Resistor ($R_{dielectric}$), which will be responsible for the loss of charge and the heat generation in the insulator producing additional thermal noise.

If we define the dielectric loss D of the material as the ratio between the power dissipated in the resistor $R_{dielectric}$ and the reactive power stored in the capacitor [38]

$$D = \frac{i^2 R_{dielectric}}{i^2 |X_c|} = \frac{R_{dielectric}}{2\pi C f} \tag{3.16}$$

and using the equation for thermal noise, we have

$$S_{dielectric}(f) = 8\pi k_B T D C_{chip} f \tag{3.17}$$

where D is the dielectric loss of the material and C_{chip} is the capacitance of the nanopore membrane and the silicon supporting structure[38–40].

3.3.4 Input Capacitance Noise

At high frequencies the ionic current noise is dominated by the coupling of the voltage noise at the operational amplifier input, with the distributed capacitances of the system, C_{total}. The operational amplifier has an inherent thermal noise in its amplifier components, which include elements that can have a resistance such as FETs. This noise is thermal in its origin and we will denote its PSD by $S_{Vin} = e_n^2$. The op-amp imput is connected with the nanopore with a capacitance in parallel. If a signal *x(t)* passes through a linear network to become *y(t)* the power spectral density is altered as equation (3.18) describes[41].

$$S_y = |H(j2\pi f)|^2 S_x \qquad (3.18)$$

For simplicity lets consider the case where there is no nanopore, just the free-standing membrane. Since the transfer function between the current going through the capacitor and the voltage at the OPAM input is just $(j2\pi f) = \frac{1}{Z} = j2\pi f C_{total}$. the PSD of the input capacitance noise is

$$S_{capacitance} = (2\pi f C_{total})^2 e_n^2 \qquad (3.19)$$

This noise can be dramatically reduced by reducing the capacitance of the whole system, which is dominated by the capacitance of the free standing membrane and the supporting structure, C_{chip}. It has been shown that painting PDMS on the chip dramatically reduces the noise at high frequencies[29]. Usually the capacitance of a painted chip is reduced from ~250pF to ~60pF. Other approaches have also been used to reduce the C_{chip} capacitance[24].

For our particular case, painting PDMS on the surface of the chip not only helps to reduce capacitive noise, but it also eliminates the coupling between the light source noise and the current noise. I will show this result in the discussion of the noise produced by the illumination source.

3.3.5 Noise Pickup

So far we have described all the inherent sources of noise of a standard nanopore system relying on ionic current measurements. I will define as Pickup Noise as all the external noise sources that contaminate the electrical response of the nanopore system, whether it is by the pick up of electromagnetic interferences by the conducting fluid in the tubes, or noise infiltrated from the power lines of the electronic equipment (e.g. Axopatch, DAQ card, etc.) The former is usually reduced by the implementation of two nested Faraday cages[24]. The latter is reduced by turning off electronic devices that share the same power network, so that the 60Hz power signal is not polluted with additional frequencies by the electronic equipment. The equipment that must remain on for the experiment should be connected into different power outlets until an optimal configuration is reached.

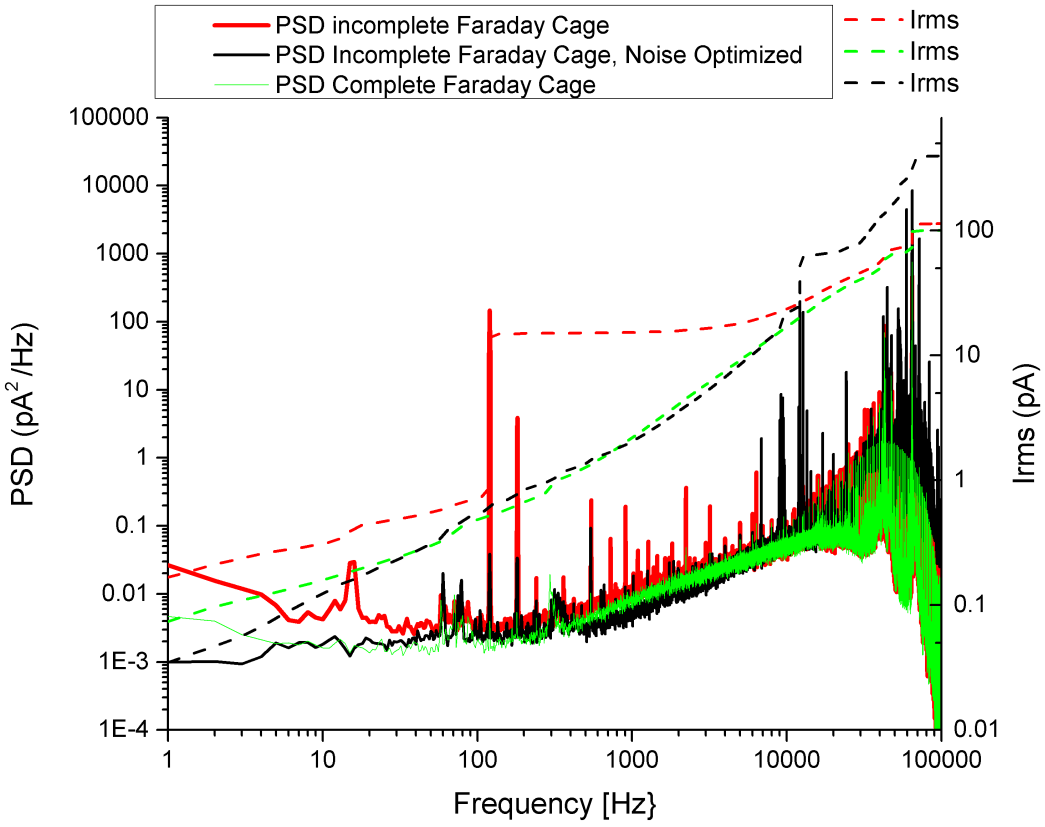

Figure 3.2 Three PSDs illustrating the change in noise performance when the Faraday cage is incomplete. Dashed lines indicate rms currents for the corresponding PSDs. Green curve PSD with Faraday cage is fully closed. Red PSD optical access opening. Black curve: optical opening and noise pickup optimized. The red and green curves were taken with device B10.6 and black curve with device B10.7. The black curve illustrates only that the 120 Hz spike can be reduced, and should not be compared to the other two. Data taken at 0mV at 3.6M LiCl σ=159.5 mS/cm, low-pass filtered at 100kHz with Axopatch 200B.

In my custom built instrument, I have identified several problems with Pickup Noise, 1) we have an opening in the Faraday cage for optical access of the microscope objective, 2) we use long tubes filled with liquid which act as antennas and receive electromagnetic waves, 3) there is a lot of electronic equipment in the

close proximity of the fluidic device which pollutes the environment with electric noise.

3.3.5.1 Incomplete Faraday Cage

The Faraday cage (See chapter 2) is not complete because an opening for optical access to the sample is needed. The opening occurs very close to the nanopore due to the working distance limitation imposed by the microscope objective. This path for pickup noise although small (~12mm), is very important due to the proximity to the sample. To test the noise impact of the incomplete Faraday cage versus the standard fully enclosed one, we completed the Faraday cage with aluminum foil and measured the noise in both situations. The results shown in Figure 2, indicate that the noise that penetrates into the Faraday cage through the optical opening is significant and cannot be neglected. There is a particularly big spike at 120Hz that appears in the opened case and the rms current increases by a factor of ~8.

To minimize this problem I enclosed all the system in a large external Faraday cage sitting on the metallic surface of the optical table to complete the shield. The Microscope, Camera, Axopatch, DAQ Card, Laser and Syringe Pump are placed inside a metal mesh with openings of about 3mm. Special attention was provided to the power cables that go into the cage since they can generate a 60Hz noise (since harmonics are present it also generates 120Hz noise) in the signal, so the oscilloscope was positioned outside of the large Faraday cage.

All the electronic equipment that could be turned off during the experiment was turned off. Fortunately, the motorized optical microscope (Nikon Ti-E) can be

turned off without losing the optical position of all the lenses inside. Once the sample is in focus, the filter cube in place and the light's path set to the camera, the microscope can be switched off. Nevertheless, this is a rather tedious procedure because once the microscope is re-initialized (turned on), it resets its configuration, and it needs to be refocused and reconfigured. The XY stage is also switched off, all the optical lamps except the laser are off. During the data acquisition I don't need to flow the analytes into the microfluidic device, hence the syringe pump is also off. The only essential electronic equipment operating inside the external Faraday cage during the experiments are: Axopatch, DAQ Card, Camera and Laser. Outside the Faraday cage we had the oscilloscope and the computer. It is worth noting that the illumination provided by the laboratory ceiling lights is also a source of noise, so the instrument and the working area nearby are closed off by black curtains to block the ambient light.

3.3.5.2 Tube noise

In the traditional nanopore fluidic cells, Ag/AgCl electrodes are placed relatively close to the nanopore, or the fluidic path between them is made with a large cross section, as to minimize access resistance arising from the liquid electrolyte. In my custom built instrument, however, I could not place the electrodes in close proximity since the AgCl surface is photosensitive and produces electrical noise in the ionic current signal upon illumination. Therefore electrodes must be placed

away from the nanopore and protected from the light source of the fluorescence microscope.

To address this issue, I have placed the electrodes in 1.5 mL glass vials positioned a couple centimetres from the nanopore (see chapter 2). Electrical contact is done by connecting the vials to the fluidic cell containing the nanopore chip with tubing filled with liquid electrolyte. Note that the nanopore fluidic cell here is a flow cell (see Chapter 2) so that these vials also serve as reservoirs to flow liquid to the nanopore chip. Considering the tubes contain a conducting solution (e.g. 0.1-1M KCl) they behave as antennas, and despite the fact that they are placed inside the internal Faraday cage they pick up noise as electromagnetic interference and contribute to the electrical noise of the nanopore system.

I have found that the length of the tubes has a big impact on the amount of noise picked up. In Figure 3.4 I compare two PSDs of the system with long tubes (30 cm) and short tubes (7 cm). We can see that the PSD is shifted up for a wide range of frequencies (up to 10kHz), and the change is about two orders of magnitude. I attribute this behaviour to two main reasons: the tubes pick up more noise as antennas, and their resistance is also increased. However, given the resistance for a tube with this characteristic (1 MΩ) the thermal noise should play a marginal role compared to the 100MΩ nanopore.

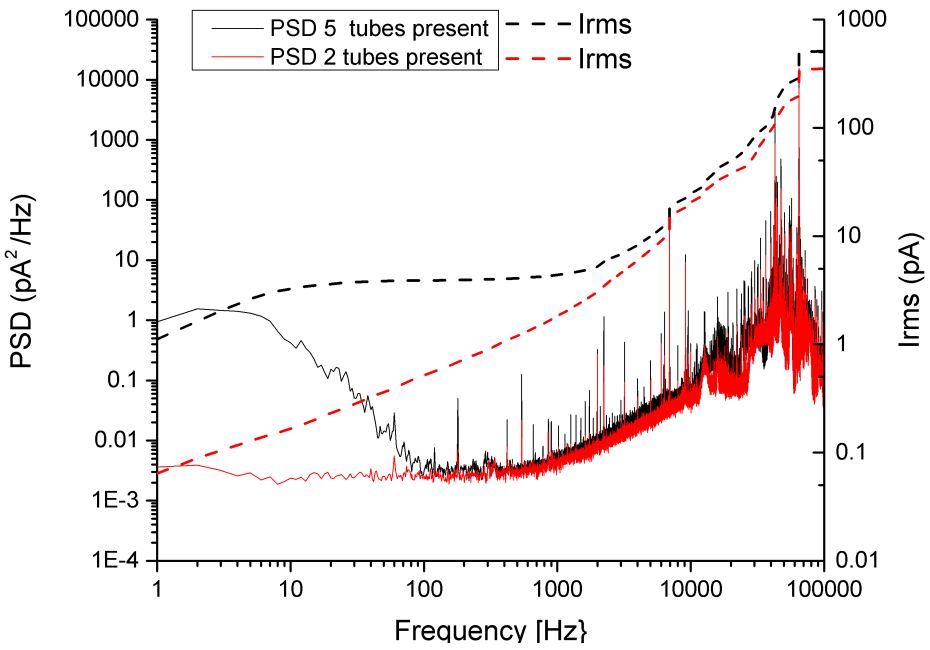

Figure 3.3 Noise introduced by redundant tubes. The microfluidic device is composed of 3 access channels for the membrane side of the chip, which are then connected to tubes; and 2 access tubes for the etched pit side. Removing the three redundant fluidic tubes from the device reduces the noise. Note how the low frequency noise is reduced and also the spikes are less prominent. The dashed lines indicate the I_{rms} for both cases. The difference is important for the low frequency range. Data acquired with a completely closed Faraday cage, no illumination, device B10.6 with no pore drilled (blank membrane), 3.6M LiCl σ=159.5 mS/cm. Data low-pass filtered at 100kHz

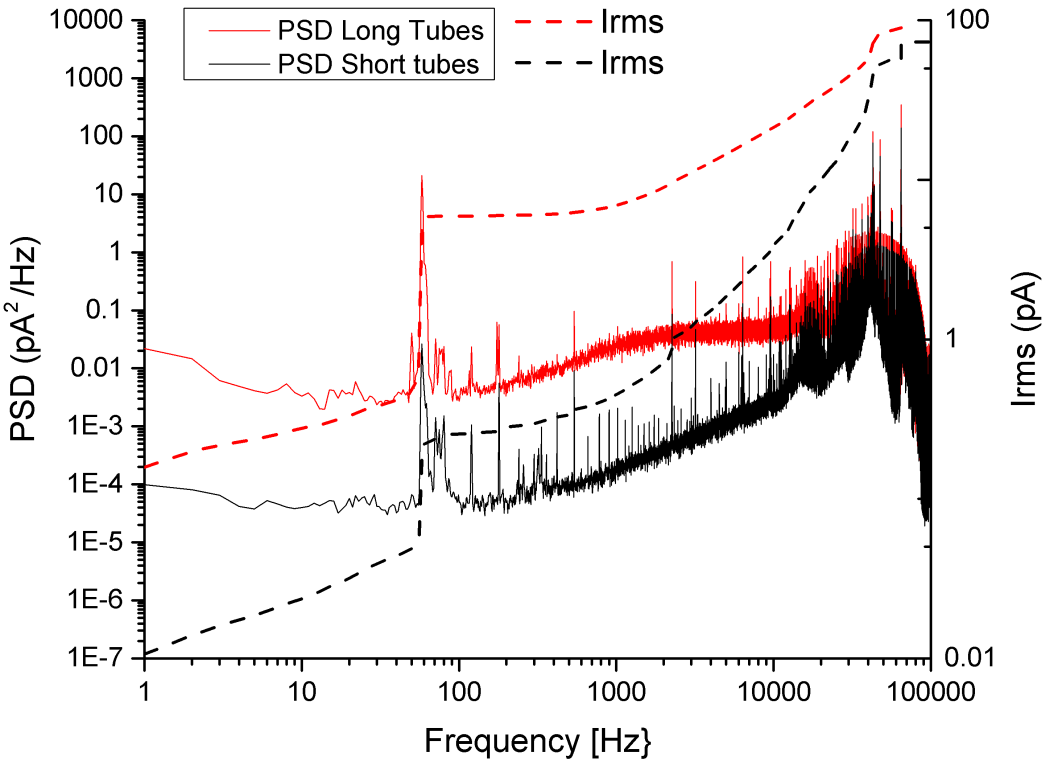

Figure 3.4 Comparison between the fluidic device with long tubes (~30cm) ; and the device with short tubes (~7cm). We see a constant shift in noise, presumably thermal noise from the tube resistance. Dashed lines indicate the I_{rms} for both cases. The big spikes at 60 Hz are there because the Faraday cage was incomplete when the data was taken, and a second external Faraday cage was not yet in use. Device B10.5 with no pore, data taken in a solution 1M KCl pH10 σ=110.6 mS/cm, low-pass filtered at 30 kHz.

Our fluidic system is composed of 3 access channels for the membrane side of the chip, which are then connected to tubes; and 2 access tubes for the etched pit side. Strictly we only need two fluidic accesses to the chip, one for each side of the nanopore. So, once the nanopore was fully wet, I didn't need to flow any more solution and the exhaust tubes were not needed, they could be removed without loosing electrical contact. The three redundant fluidic tubes from the device were

removed and the consequence is a clear reduction in the noise on the low frequencies as seen in Figure 3.3. Note how the low frequency noise is reduced and also the spikes are less prominent.

Trying to shield the tubes with grounded aluminum paper did not prove to be helpful. The Al paper seems to introduce vibrations transmitted to the electrodes, which produce a low frequency noise. This type of noise will be treated in section 3.3.6

3.3.6 Electrode Noise

A pair Silver-Silver Chloride (Ag/AgCl) electrodes is used to create an electric field in the proximity of the nanopore. The electrodes reversibly transform ionic current into electronic current. Electrodes in the setup can be responsible for low frequency noise. They pick up acoustic vibrations. To minimize electrode noise it is advised to mount the nanopore instrument on top of an acoustic table to minimize vibrations coming from the floor[24]. Traditionally, electrodes are clamped to avoid vibrations, kept as short as possible to avoid extra resistance of the silver wire and placed in close proximity of the nanopore to reduce access resistance.

In our system that is impossible: they have to be far away from the nanopore to prevent light from reaching them and influencing the electrochemical reactions. On the other hand, they must be long because they are immersed in vials for electrolyte solution, and the level of solution varies widely. If the electrodes are

short and just touching the solution eventually they will lose electric contact with the solution as the level is lowered.

This particular condition makes the electrodes more prone to vibrate. Vibration on the electrodes is significant in the low frequency range. In Figure 3.5, we can see two different situations: the electrodes are inserted into the silicone septa (red) and they have a piece of adhesive tape on top which secures them poorly and increases the vibrations (black).

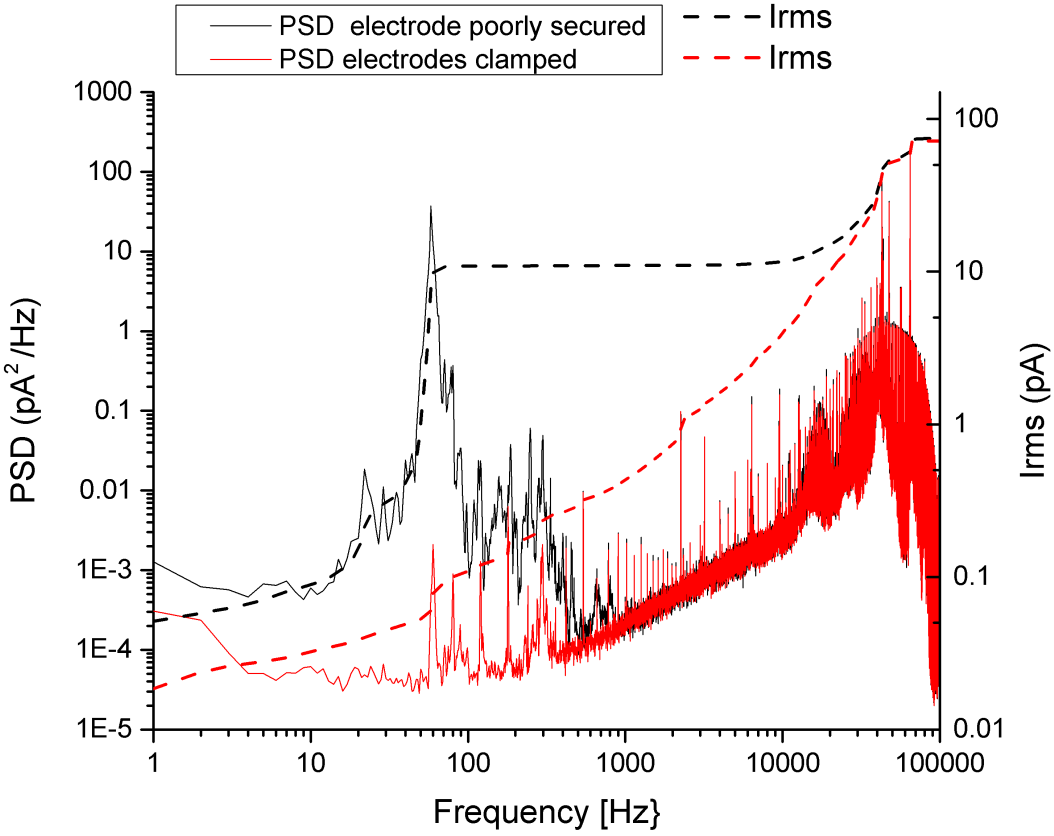

Figure 3.5 Electrode Noise. PSDs of the system with the electrodes secured in two different ways. In the black curve there was a scotch tape on top of one electrode securing it badly. The tape increased the mechanical vibrations of the electrode and the noise over all the frequencies from 1Hz to 1kHz is increased. In the red curve, the tape was removed and the electrodes secured to the vials.

Device B10.5 with no pore. 1M KCl pH 8 σ=108.0mS/cm, low-pass filtered at 30 kHz.

It can be seen that the noise is actually increased, as an adhesive tape is present. The silicone apparently damps the vibrations of the electrode and improves performance.

Acoustic noise can sometimes be present. In such cases the instrument becomes very sensitive to acoustic noise and it translates all the sounds into the current, (resembling a microphone). In my experience, acoustic noise disappears when the solution is properly degassed and the fluidic cell is vacuumed carefully to prevent bubble formation inside the channels and tubes.

3.4 Noise produced by the illumination source

The reduction of the noise produced by the interaction of light with the nanopore chip has played a fundamental role in the development of this instrument. I have seen that upon illumination, the nanopore system noise increases significantly. I attribute this noise to several potential mechanisms: 1) the photoconductivity of the substrates (Si and SiN_x),[42,43,44] 2) the alterations in surface charge on the free standing membrane and the silicon nitride situated above silicon of the rest of the chip[45 45], 3) the generation of precipitates and other chemical products facilitated by illumination[46,47], 4) photosensitivity of electrodes[24].

For the second two reasons we can readily discard them since 3) we don't have any chemical products that will precipitate easily and 4) electrodes are kept very

far from the laser source, enclosed in a metal holder to prevent light leaking into them. I will discuss the remaining mechanisms of noise generation next.

3.4.1 Photoconductivity

Photoconductivity is a direct result of the photoelectric effect. A photon with energy $h\nu > \Delta E_{bandgap}$ will be capable of exciting an electron from the top of the valence band, to the conduction band. The minimum wavelength for this transition to occur is given by[44]

$$\lambda = \frac{hc}{\Delta E} \tag{3.20}$$

where λ is the wavelength, h is Plank's constant, c is the speed of light and ΔE is the change in energy . In the case of silicon, light with a wavelength smaller than 1.12 μm will generate electron-hole pairs

The main difference between Si and SiN_x with respect to photoconductivity is their band gap. If the Si chip is illuminated, a photon from the laser source (λ=488nm, E=2.54eV) can easily create an electron-hole pair, since the band gap of Silicon is 1.1eV. The thin layer of silicon nitride that has been deposited on the silicon chip, does not prevent light from reaching the silicon since SiN_x is transparent to most visible light. Given the fact that the band gap of SiN_x is considerably bigger than the band gap of Si, photoconductivity should be present to a lesser extent. However, the band gap of SiN_x depends on the ratio of N/Si. It naturally approaches the band gap of pure Si, as the concentration of Si dominates over the concentration of N,

and increases up to ~6eV when N/Si=2. [43] If the ratio is 0.8, the band gap of SiN_x is ~2.4eV. The photons on our laser have energies of 2.54eV, so charge carrier generation may be present.

To investigate the behaviour of the illuminated chip, I have characterized its conduction as a function of laser intensity on a membrane with no pore. The result showed that the conduction indeed has an increase when we illuminate the chip with a high power (50mW). However, this increase was only evident for voltages above 6V (it increased by a factor of 3 for 8V), which we will not be using. I tried to measure the conduction on ranges from -1V to 1V but the results were not meaningful since the current was minute.

However, light undermines the dielectric properties of silicon nitride and increases its dielectric noise. Even if current tunnelling through the membrane is negligible, dielectric noise is a known phenomenon[24], and illumination will make it worse. This argument is supported by an increase in noise in the dielectric region (100Hz -3000Hz) upon illumination.

3.4.2 Surface Charge fluctuations

In addition to the photoconductivity effect, illumination of the SiN_x changes its surface charge[45]. SiN_x has a pH dependent surface charge that screens on the solution forming an electrical double layer. The sudden surface charge change produced by the light creates a transient capacitive spike. The current spike is observed in reverse direction when illumination is stopped. This constitutes a

coupling mechanism between the light and the current. Any fluctuations in the intensity of light will cause corresponding fluctuations in the current though the nanopore.

Due to surface charge alterations, any pulsed light source is unusable. A mercury arc lamp was initially installed (X-Cite 120 PC, EXFO), the wide spectrum illumination produced by it was filtered with a FITC cube filter (excitation, 485-490nm emission 510-536nm) to excite YOYO-1 dye attached to the DNA. The light bulb of the lamp is powered with an AC voltage, and the light intensity varies accordingly. The dramatic changes in intensity are reflected into the electric signal, which displays very high current peak at 300 Hz. The current trace displays a periodic feature that we attribute to the way the mercury bulb is driven by the electronics of the lamp. The rms current noise at 10kHz of the system when this lamp was used was ~450pA. If one assumes Gaussian statistics the peak-to-peak noise should be ~8 times the I_{rms}, so a peak-to-peak noise is 3600pA, 3.6 times the maximum possible blockage. With such a signal, electrical detection of DNA molecules on the nanopore becomes impossible.

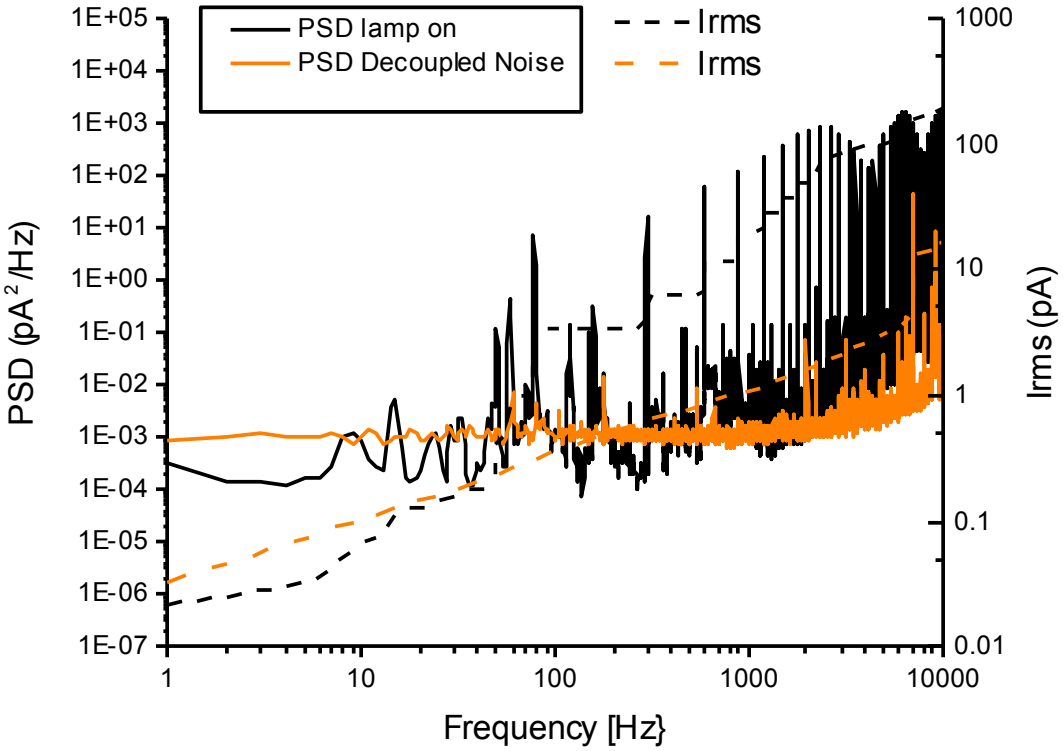

Figure 3.6 Illumination noise by a pulsed light source. Two PSDs showing the change in noise performance when the system is illuminated with a pulsed mercury arc lamp (black) and when the noise has been optimized (orange). The pulsed light couples with the current and the current signal displays periodic features that translate to harmonic spikes on the PSD. The rms currents are shown in dashed lines for each case. Device NY01.3 with a 41nm pore. Data taken in 1M KCl pH 8, σ=110.6 mS/cm low-pass filtered at 30kHz

Once we identified this surface-charge coupling mechanism it became evident that we need to characterize the noise on our laser. I used a fast photodiode to characterize the laser diode and I found that it is only stable at powers P >20mW, (the laser is designed to work at 50mW)

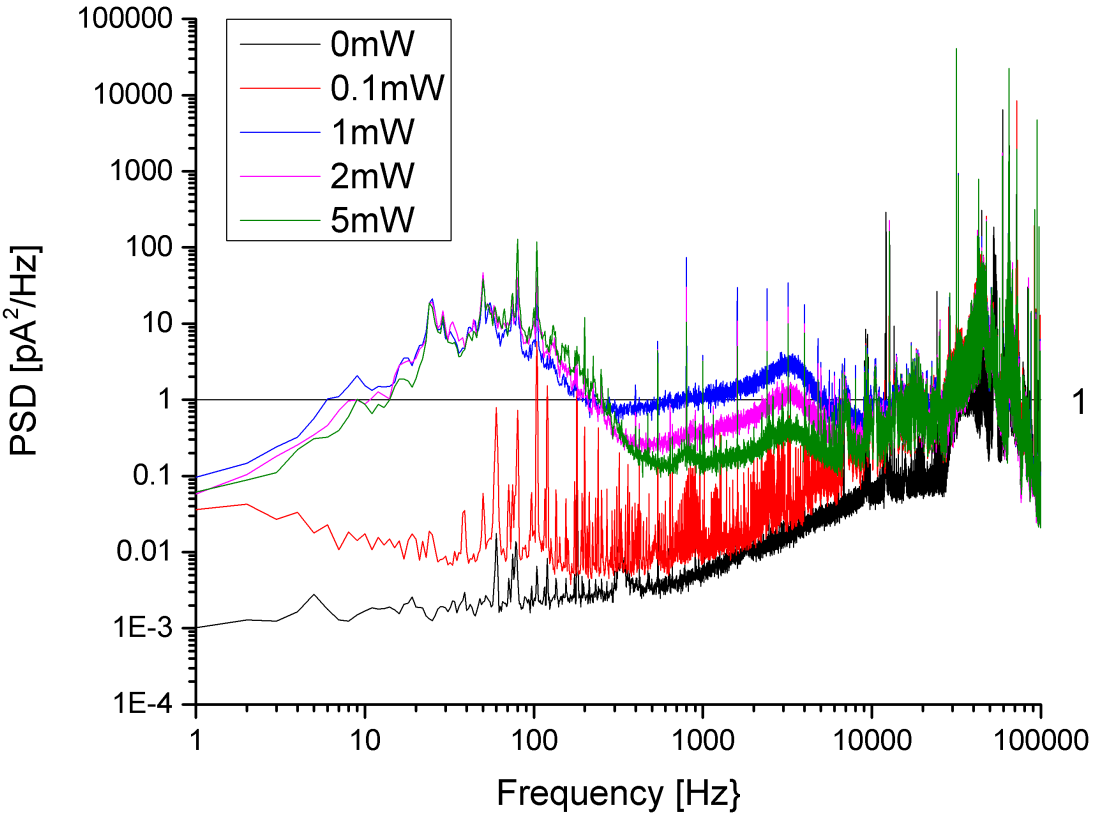

Figure 3.7. Noise produced by various laser illumination powers. PSD of the system with different illumination powers. The laser is illuminating the membrane and part of the supporting structure from the silicon chip. We see a low frequency noise appear from 3 to 300 Hz, which saturates after 1mW and remains the same for powers above. Interestingly there is a peak in the noise at 3 kHz, which is reduced as power increases. Device B10.7 with no pore. Data taken in 3.6 M LiCl pH 8 σ=159.5 mS/cm, low-pass filtered at 100kHz.

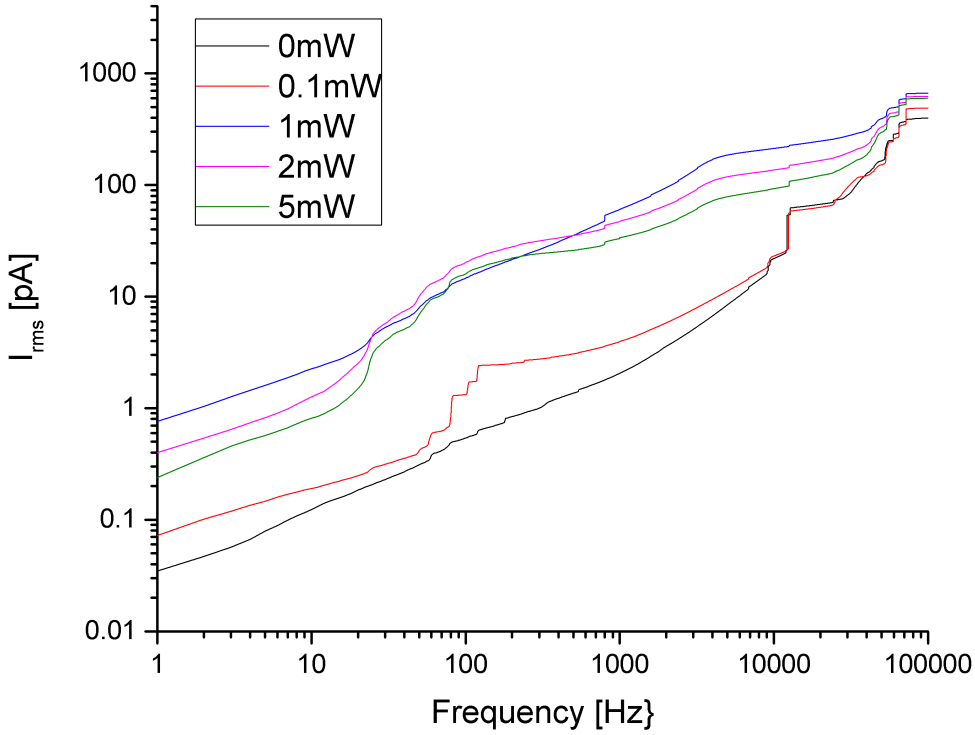

Figure 3.8. I_{rms} calculated as a function of frequency for various laser powers (from the data in Figure 3.7). I_{rms} =200pA at 10kHz for P=5mW. The Laser is illuminating the membrane and part of the supporting structure. Device B10.7 with no pore. Data taken in 3.6 M LiCl pH 8 σ=159.5 mS/cm, low-pass filtered at 100kHz.

The noise characterization of the system when the laser is working at low powers can be seen in Figure 3.7 and the rms current produced in Figure 3.8. One notices a big increment in noise as the laser power is increased (from 0 to 5mW).

It was necessary then to attenuate the power in a different way. I implemented an optical attenuator (see chapter 2) with good results.

In the implementation of the optical attenuator these aspects of the incident light changed:

1. The laser is operated at the power it is designed for (50mW)
2. The light reaching the membrane was very well polarized (extinction ratio 1:10 000)
3. An intermediate mirror was removed from the light path, which might have vibrated and caused a vibration on the incident light.

I believe that the first and the third play an important role. Laser stability is very important for the current recordings, and stable optical mirrors prevent the laser beam from vibrating. Both will result in intensity fluctuations of the incident light. Such fluctuations will couple to the current noise with a mechanism discussed in sections 3.4.1 and 3.4.2. As for the second (laser polarization), I could not find a clear correlation between the noise performance and polarization of the incident light.

The noise measurement after the installation of the optical attenuator is shown in Figure 3.9. All the low frequency fluctuations have been removed, and the only spikes remaining are in the range of 60 Hz. We also see a plateau ranging from 100 Hz to 3kHz, with a very small spike at 3kHz. This spike is on the region of dielectric noise and should be due to the diminished dielectric properties of illuminated silicon nitride and silicon.

The RMS current reduction is evident; it is reduced from 200pA (with no attenuator) to 39pA at 10kHz

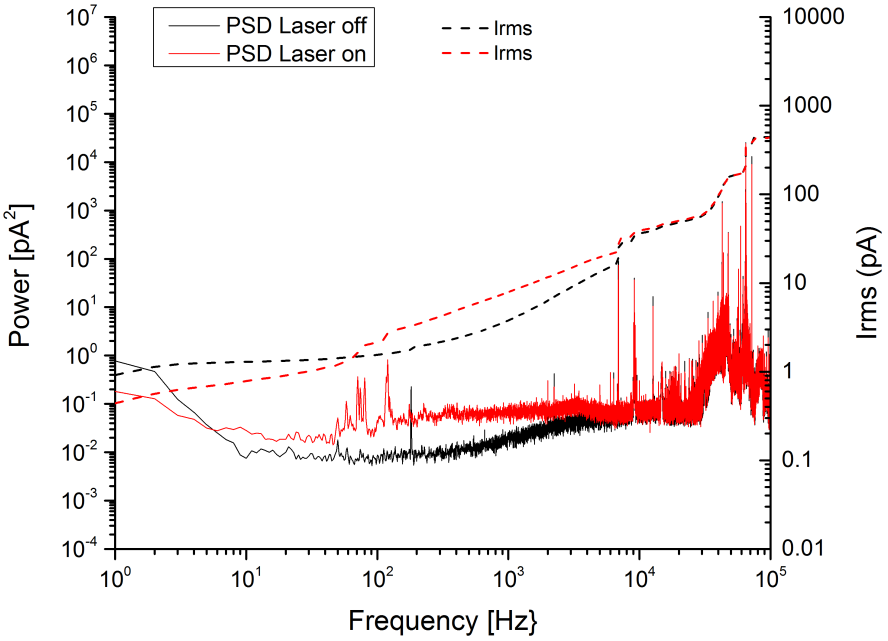

Figure 3.9 Illumination Noise with an optical attenuator. Comparison between PSDs and I_{rms} under illumination (red, I_{rms} =39pA) at 4.25mW and in the dark (black). All the low frequency noise has been removed. Data taken in device B11.1 with a 40nm pore in 3.6M LiCl at 0V.

This noise level is closer to what should be required for DNA electrical detection. However, if the noise coupling from the laser into the electrical system is a surface, effect, the natural question to ask is: is there a way to remove the contact of the surface of the chip and the electrolytic solution? Fortunately the answer is yes.

3.4.3 Illumination noise decoupling

I used the technique previously reported by Tabard-Cossa et al[29] to reduce capacitive and dielectric noise. They painted PDMS on the chip surface aiming to cover the entire chip except for the freestanding membrane. PDMS was painted in this way on device B12.1. Fortunately, the PDMS on top of the chip does not affect

the fabrication process. PDMS was also painted on the back (etched pit side) of the chip to minimize contact of the electrolytic solution with the silicon.

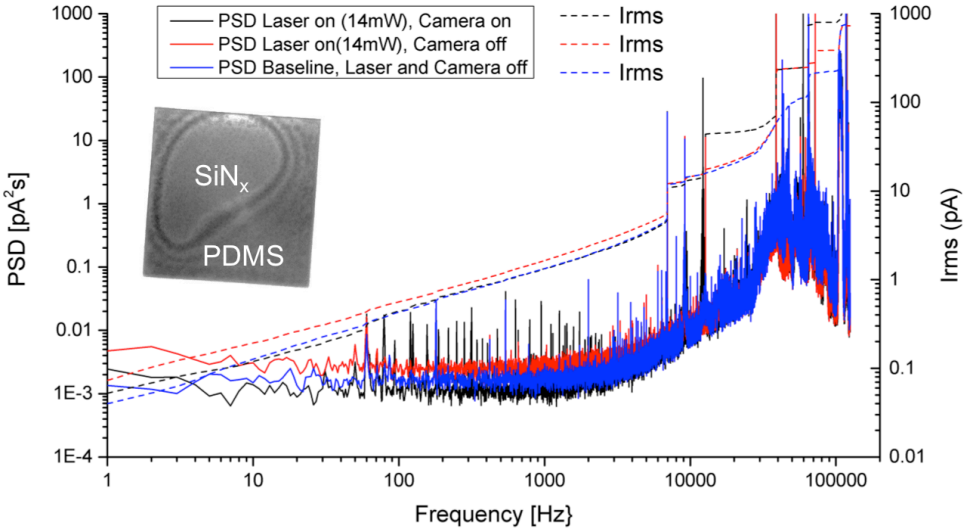

Figure 3.10 Illumination noise decoupled from the nanopore based optofluidic device. The baseline (best case scenario) with all the electronics, the laser and the camera off is shown in blue. The red curve shows the noise of the system when the laser is on at 14mW (power higher than our needs). One element, which does introduce some noise, is the camera (black curve). The rms current noise with all the optical system functioning is ~10.8pA at 10kHz. Device B12.1 at 3.6M LiCl with a 4.5nm pore.

Other systems have seen a noise performance very similar to that one which we have optimized. Two phenomena should be taken into account to propose a mechanism for the illumination noise.

First, as discussed previously, illumination of silicon nitride produces electron-hole pairs which increase conductivity of the substrate and undermine its dielectric properties. Hence dielectric noise plays a more significant role in the noise

performance than in non-illuminated membranes. This argument is supported by an increase in noise in the dielectric region (100Hz -3000Hz) upon illumination.

Second, Di Fiori *et al.*[48] report an increase of noise upon illumination. They don't specifically treat noise but propose that the enhanced conductivity of a nanopore when it is illuminated is caused by a change in surface charge due to silicon nitride dangling bonds[42,43]. When the laser is turned on or off, a spike very similar to a capacitive spike is seen on the current signal, suggesting a surface effect.

I hypothesise that upon illumination, charge is liberated from the membrane surface in a similar way as a capacitor discharging. The dangling bonds of silicon nitride are not a definite explanation of the noise generation, but they provide a coupling mechanism between fluctuations on the laser intensity and the current through the pore.

Painting PDMS on the entire chip except the freestanding membrane reduces both effects: it covers the vast majority of silicon nitride surface, so that surface effects are not of importance. It also increases the dielectric properties of the chip and reduces dielectric noise.

Interestingly enough, the noise performance on this device (with PDMS painted on all the chip but the membrane) did not depend on the laser intensity (Figure 3.11). The noise performance did not change with a change in power, which is very convenient from an experimental point of view. It also suggests that the coupling

mechanism between the laser fluctuations and the current has been significantly reduced.

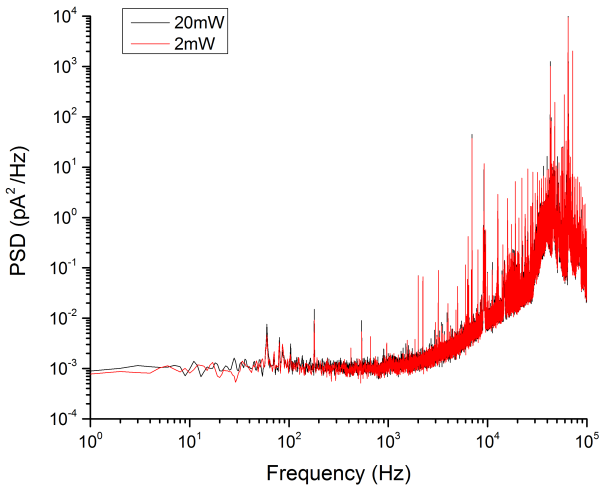

Figure 3.11 Noise performance of a PDMS painted chip with two illumination powers. One can see that a factor of 10 increase in illumination power does not have any visible effect on the noise performance**.**

There is evidence proving that the noise from the illumination source has been decoupled from the electrical measurements, and the electrical detection system under illumination has a sensitivity and resolution that approach the regular nanopore systems, which do not feature optical measurements.

The only aspect that should be further optimized is the noise introduced by the camera. I will discuss this issue in the outlook section.

4 Preliminary Results and Outlook

In this chapter I will discuss the main results obtained with my custom nanopore based optofluidic instrument towards performing simultaneous detection. Firstly, I will discuss the results on electrical detection of DNA in the microfluidic system. The results obtained with the optical system will be presented next. I will discuss 3 features: the optimization that has been done to maximize the optical contrast, the results of visualization of free floating DNA in solution and the optical detection of translocation through nanopores. Finally, an experiment demonstrating that it is possible to detect DNA electrically when all the optical detection system is working will be shown. Such an experiment is evidence that the noise levels produced by the optical measurement are sufficiently low to perform electrical detection. In the outlook section preliminary results on the localized laser enhanced dielectric breakdown will be presented. Finally, I will close this chapter with an outlook on

the next steps that need to be taken to further optimize the presently operational instrument.

4.1 Electrical Detection of DNA

Electrical detection was the first control that needed to be done in order to ensure that the electrical system was fully functional. The noise floor of the purely electrical system was characterized and shown to be equivalent to other standard nanopore systems in the lab (see Chapter 2). The characterization was done by replacing the microfluidic PDMS cell, by regular Teflon cells used in standard setups. The pores fabricated in the regular cells exhibited very low noise, even when mounted in the optofluidic instrument, indicating that the noise was in the same conditions as other regular nanopore setups in the lab. In addition, this control helped to fine tune the protocols to detect DNA in several conditions, especially at the concentration of 100mM KCl at which DNA-YOYO-1 complexes are stable.

4.1.1 Detection in PDMS microfluidic cells

A second test needed to be done with the microfluidic cell. I was concerned that the violent flow created in a fluidic channel upon injection of the solution would interfere with the DNA translocation, or the pore's integrity. The experiment showed that flow can be controlled and it can be brought to a level such that it will not prevent translocations and pore's stability was acceptable.

After a few attempts, I was able to detect DNA on a microfluidic cell, in a 6nm pore at 1M KCl, with a DNA concentration of 10 μg/mL of 10kbp DNA. The optical system was not functioning during detection. Blockages from 10% to 20% were detected as shown in Figure 4.1 and Figure 4.2

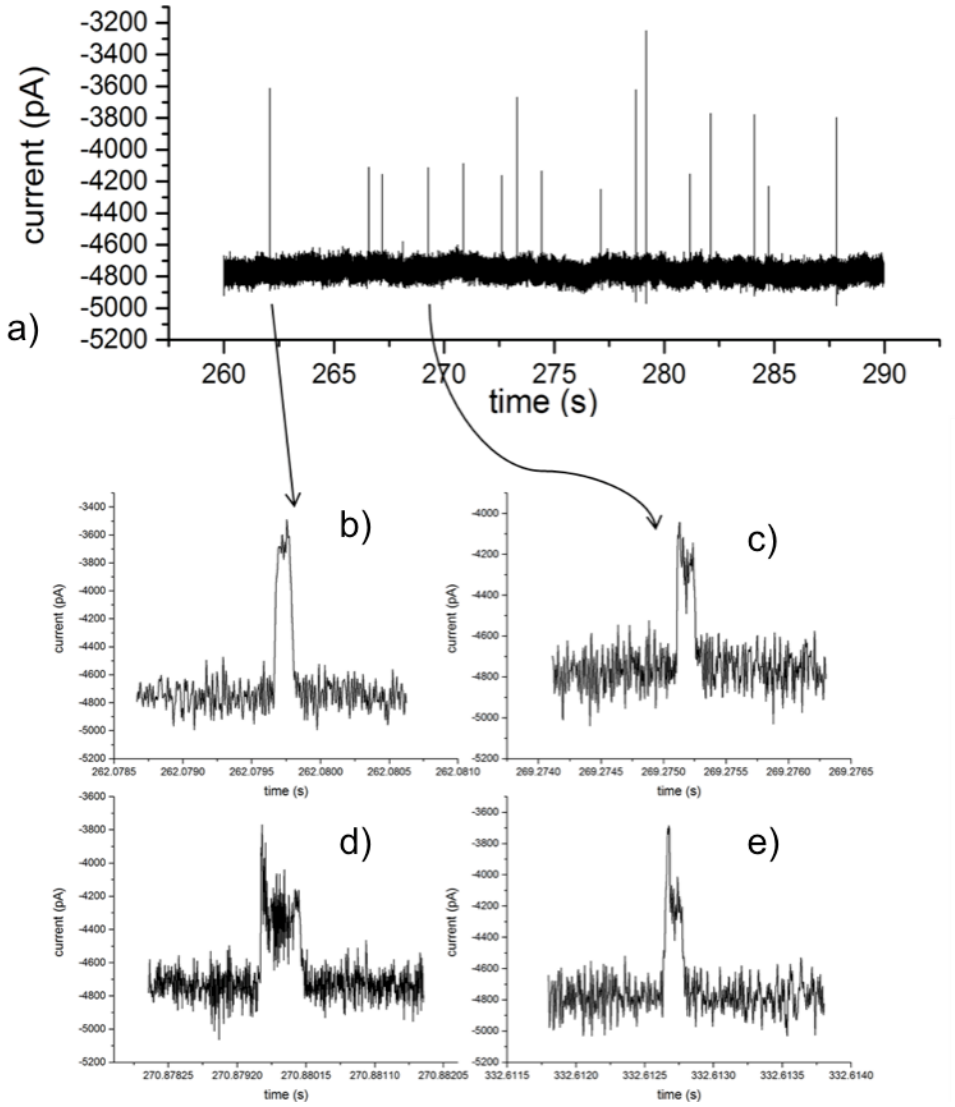

Figure 4.1 Translocation events in the microfluidic PDMS cell. a) 30s of current trace is shown with blockage spikes corresponding to DNA translocation events. b-e) Individual translocation events are shown with different features, d) e) two levels correspond to a folded state and b) c) single levels correspond to single file translocations. A negative voltage is applied with a corresponding negative current, so that upward spikes are blockages. A d=6nm, L=30nm pore was used in

1M KCl (σ=127.5 mS/cm), 337mV was applied. 10kbp DNA was used and the data was low-pass filtered at 30kHz, with a four pole Bessel filter. Device B06.2.

DNA can thread through a 6nm pore either in a single file, or in a folded state. Thus, two blockage levels are expected. In Figure 4.1 d) e) are folded events and b), c) show single levels corresponding to single file translocations.

Equation 1.3 can be used to estimate the value of the current change, using the values $\sigma = 127.5\ mS/cm$, $d_{DNA} = 2.2nm$, l=30nm, and V=337mV

$\Delta I = -\frac{\sigma\pi d_{DNA}^2}{4l}V$=-0.54nA

which match the observed translocation blockage for the first level (~0.5nA), suggesting that DNA was actually detected.

For all the translocation events, a plot of the percent blockage vs. the translocation time is shown in Figure 4.2. Since all the molecules were identical in length (10kbp) one will expect that folded events will take shorter and single file events will have a higher dwell time. This is confirmed by the fact that there are two groups of events: those under a blockage of 12% and those with a higher blockage. It is evident that translocations with a higher percent blockage, take less time to translocate. On the other hand, single file events are dispersed, over a wide range of times.

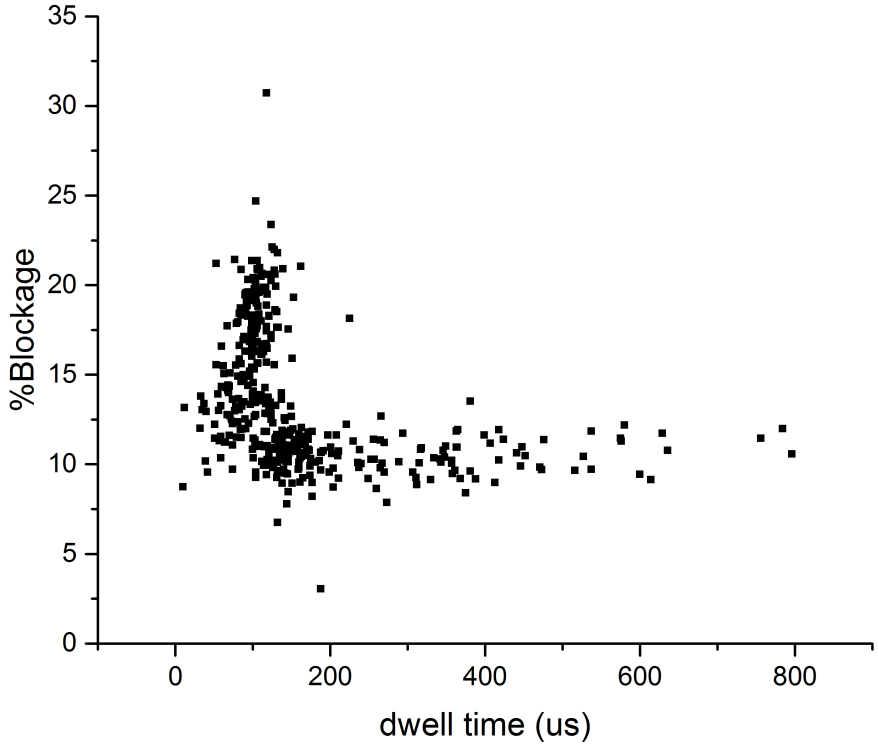

Figure 4.2 Scatter plot of the %Blockage *vs.* dwell time for the translocation events. Low blockage events (<12%) correspond to single file translocation and extend over a wide range of dwell times. Higher blockages are shorter since the molecules translocate in a folded state and take less time to thread through the pore. A higher blockage corresponds to low dwell time as expected.

4.2 Optical Detection of DNA

I tested different methods to stain the DNA. I stained it with YOYO-1 dye (Life Technologies), SYBR Green (Life Technologies) and we also tried to attach fluorescently labelled dUTps-12-fluorescein (Thermo Scientific) to a 5kbp DNA strand via PCR. SYBR green stained the DNA but free-floating dye also fluoresces, (YOYO-1 only fluoresces when bound to DNA) so the optical SNR is compromised. As for the PCR product, I could not see any DNA molecules, even though we had evidence that DNA was produced in the PCR reaction, there were either no

fluorescent dUTPs attached to the DNA, or there was an excess of free floating dye which was not removed in the cleaning process, and made impossible to distinguish the DNA.

The only way I was able to see DNA consistently was staining it with YOYO-1 dye. The commercial protocols I tried to stain DNA did not yield good results. Usually, the dye is mixed with DNA in a TE buffer. I found that the dye did not attach properly to the DNA. Nevertheless when the dye is incubated together with the DNA in DI water for a period of time (90min at 50 ° C) it attaches very well, and then it can be mixed with 100mM KCl or with TE buffer.

4.2.1 Optimization of contrast for fluorescent detection

I will discuss several factors that influence the contrast. Firstly, the concentration of DNA is critical to achieve a good optical signal. Clearly, if too many molecules reside in the illumination volume, light from all those molecules will be collected. The light of those molecules, that are not in the depth of focus region, will blur the image. On the other hand, it is necessary that all the elements that are illuminated do not fluoresce, except for the DNA.

4.2.1.1 DNA concentration

To achieve a reasonable signal to noise ratio, the concentration could not be held at the same levels as in a normal DNA experiment (2μg/50μL) which gives a concentration of 61nM for 10kbp DNA. The concentrations that allow seeing

individual molecules and still get a significant capture rate (1 every 3 seconds) are in the order of 30-60pM. Of course, the low concentration can be a factor to low capture rate and few translocations. A method that worked well in my particular experimental setup is to use a concentration gradient: one of the vials had a high concentration of DNA, and another one had no DNA. Depending on the contrast the solution with DNA was allowed to flow from one vial to the other to fine tune a concentration low enough to distinguish individual molecules (no overlap) and high enough to have captured events.

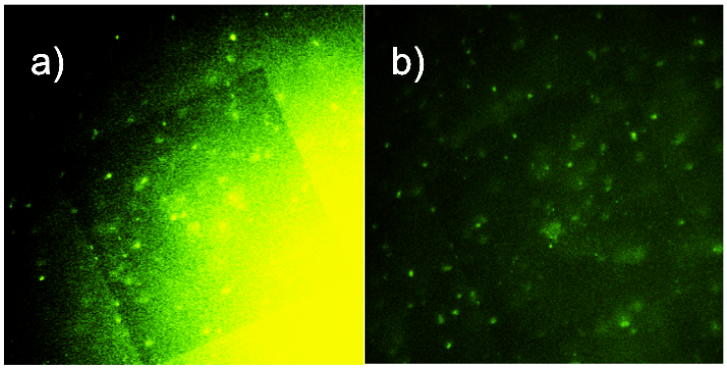

Figure 4.3. Background Fluorescence reduction. The concentration of Stained DNA is a critical factor for the optical signal. On the two images of the same device, a 50x50um membrane is shown. Every bright dot is a single λ-DNA molecule (48900 bp). a) An image with a DNA concentration gradient showing that a high concentration can make the whole field of view bright and prevent measurements. b) Once the concentration is low enough, the contrast becomes sufficient to resolve single molecules.

4.2.1.2 Autofluorescence of SiN_x and Polyether Ether Ketone (PEEK)

It has been reported in literature that SiN_x has a high autofluorescence[49]. In my experience, the fluorescence of SiN_x itself was not significant as the

autofluorescence of the material behind the SiN_x. In fact, the fluorescence of SiN_x was not detectable after a proper PDMS cell was used behind the chip. The first attempts to see DNA were done with a PEEK fluidic cell where the microfluidic device was embedded. The membrane and this cell led to a very high apparent fluorescence of the membrane, however, it went away when the PEEK was removed from behind the cell, and the complete PDMS cell was used.

Figure 4.4 shows a comparison between these two scenarios under similar circumstances. Fluorescent molecules are also shown to give a reference of the intensity level necessary to resolve single molecules.

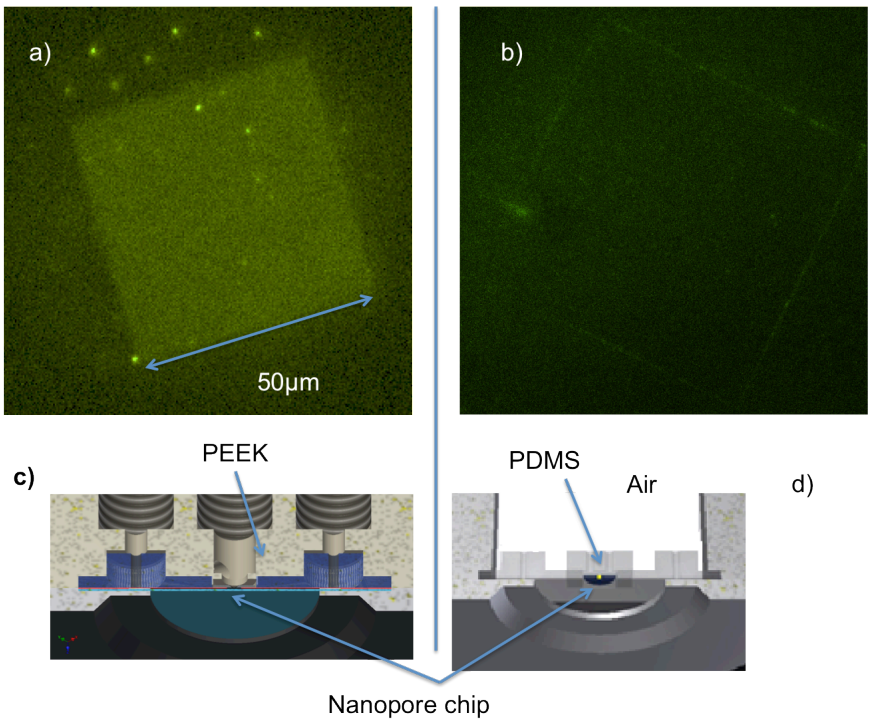

Figure 4.4 Optimization of Contrast. Images of the contrast of free-standing membrane and chip. a) Image produced by the design in c): a PEEK cell used to house the microfluidic device; it constitutes the fluidic reservoir of the back of the chip. Fluorescence and reflections from the PEEK cell behind the chip makes

membrane appear brighter. Stained DNA molecules can also be seen for intensity comparison. b) Image taken in the PDMS housing that I developed, the background in the membrane region is as good as that for the silicon. The design is shown in d) the chip has just a layer of transparent PDMS behind it, and air behind the PDMS layer. This minimizes reflections. The brightness of the membrane is not present anymore. Both pictures were taken in similar conditions.

4.2.2 Visualization of free floating DNA

Free-floating DNA was visualized and some interesting features were observed. First, the random diffusive motion of DNA can be seen on the free surface, if the flow is properly reduced. Molecules are observed to adopt different configurations while in solution. Second, DNA interacts with the surface of the silicon nitride, it seems to feel attracted to it and when molecules are close to the surface the DNA can be observed to drift and roll on the surface. Some preferred binding sites were observed: upon the application of an electric potential on the membrane molecules will stick to these places and remain there until the flow of solution is increased to the point that it detaches the molecule from the binding place. However, molecules were also observed to stick to the membrane permanently. The flow was not enough to detach them, (the molecule would just elongate) nor the application of strong reverse electric fields. These binding sites could be of interest to explain clogging or anomalous events, since molecules permanently stock to the surface could thread through the nanopore and clog it.

Figure 4.5 shows the trajectory of a DNA molecule as it moves on the surface of the membrane. For the first row, each image was taken 31ms apart. Time is expressed as a multiple of a constant t_0, where t_0=31ms. The shape of the molecule is

observed to fluctuate as it is carried by the solution flow. The fluctuation in conformation is observed by an apparent change in form and brightness of the molecule. The DNA is very close to the surface, so that the surface of the SiN_x can affect its properties. The molecule chosen is a typical example of movement of λ-DNA on the membrane surface.

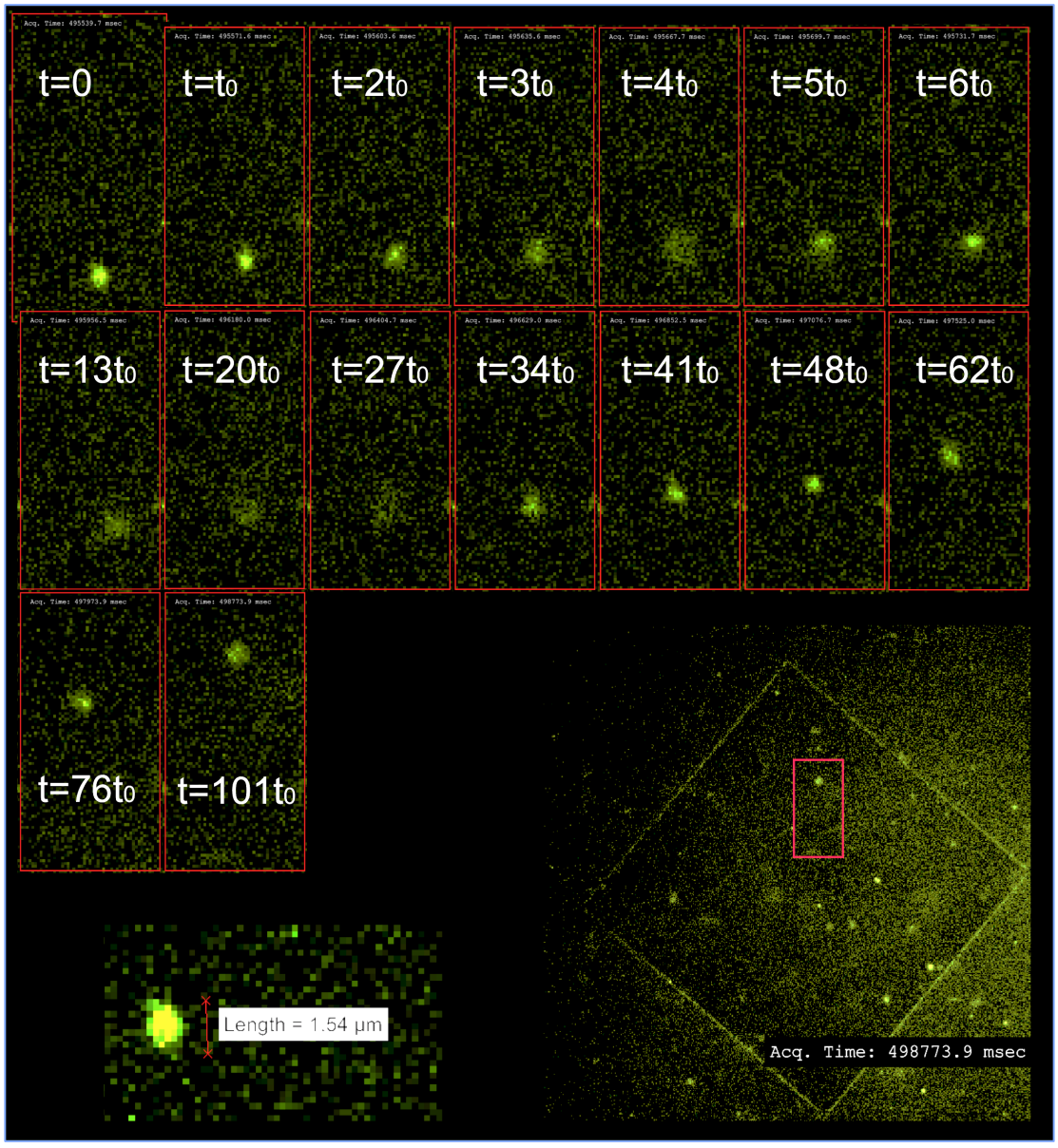

Figure 4.5 Trajectory of a DNA molecule as it moves on the surface of the membrane. For the first row, each image was taken 31ms apart (t_0=31ms). For the

second row frames are shown with a larger interval; indicated as a multiple of t_0. The inset shows the region of the membrane where the molecule was moving. The radius of gyration is estimated on the lower left corner. Lambda DNA stained at a ratio of 1/10 molecules / bp.

4.2.3 Clogging and visualization of capture dynamics by a clogged pore

The location of the pore was detected by clogging it with fluorescent molecules. A bright spot on the membrane appears after the application of a voltage. This bright spot behaves as a sink of molecules, it captures all the molecules that come close to it, and when 0V are applied, the captured molecules diffuse away. The process is reversible initially, but eventually molecules are permanently stuck at the pore location.

Clogged pores can still capture DNA, which diffuse near the pore until a circle of a particular size is completely bright. The size of this circle (which in reality could be a hemisphere) is presumably determined by the capture radius of the pore, given by the expression [50]

$$r = \frac{d^2 \mu}{8lD} \Delta V \tag{4.1}$$

where r is the capture radius, μ is the mobility of DNA, d is the diameter of the pore, D is the diffusion coefficient, l is the length of the pore, and ΔV is the voltage applied. I use data from[51] ($D=7\times10^{-13}$ m^2/s, μ=4.1e-8 m^2/Vs) and the size of the pore in Figure 4.6 (d = 7nm) to get a capture radius of r = 9.5 μm. This calculated value is twenty times higher than the measurement. The discrepancy can be explained by the obvious fact that the pore is clogged, its effective area has changed and it does not agree with the model for an unclogged cylindrical pore

because the electric field on the pore has been distorted. Nevertheless, this behaviour raises interesting questions about the nature of clogged pores.

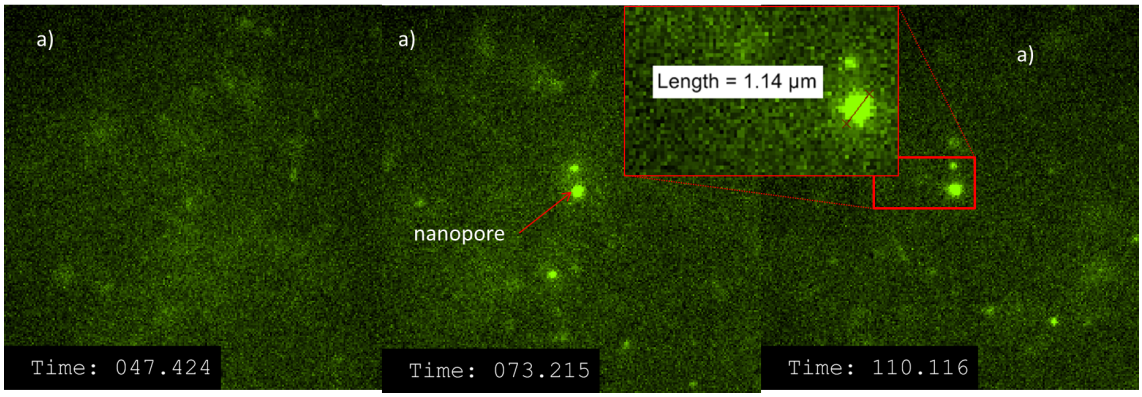

Figure 4.6 Clogged pore capturing molecules. A clogged nanopore captures DNA molecules and concentrates them near it. This forms a bright spot, which grows gradually, until a stable size is reached. Device NY01.5 with a 7nm pore at 100mM KCl. λ DNA- YOYO-1 complexes are shown.

At the time these measurements were done, electrical detection of translocations was not possible because the noise was not yet optimized. From the pure optical signal it is difficult to know if the pore is completely clogged, partially clogged, or if the bright spot is a result of the accumulation of DNA before translocation[52]. Previous studies show images of pores with a bright fluorescence spot similar to the one shown in Figure 4.6 and they still detect translocations[20], which suggests that the bright spot is either an accumulation of DNA or the pore is partially clogged. However, such behaviour should not be present for large pores, since translocation should happen immediately after capture. Experimentally, I have observed that even in large pores (d = 40nm) the pore still exhibits a bright spot (larger than for smaller pores) so the conclusion is that such accumulation of fluorescently labelled DNA happens due to clogging.

At the moment, it should be very easy to find an explanation for this behaviour, since the electrical measurements are functional. In this experiment, where salt concentration has to be lower than 100mM KCl, the DNA signals are weak but a signal to noise ratio of 1 should be possible. With the synchronized low noise current measurement that the optofluidic instrument has presently, I anticipate we will be able to clarify the issue, which would fulfil one of the objectives of the project and contribute to broaden the understanding of clogging.

4.2.4 Optical detection of translocation

On the first pore created with localized light enhanced dielectric breakdown, (See section 4.5) I was able to detect translocation optically. I speculate that light shinning on the pore during fabrication alters in some way the surface chemical composition and makes the surface less prone to stick to DNA-YOYO1 complexes (please note that more experiments are needed to confirm this claim).

On this particular experiment translocations were observed optically. Two examples are presented Figure 4.7. This pore was fabricated at the centre of the membrane as can be seen in a). The molecules approach this spot and get captured, then they diffuse away at the trans side and disappear. Hundreds of such events were observed. One example is shown in detail in part b). The molecule approaches the nanopore, it is constrained so that its free-floating shape is concentrated in a smaller radius and then it diffuses away. What is observed in the microscope, at real time resolution, is that the molecule is captured and it disappears from the field of view. The pore acts effectively as a sink.

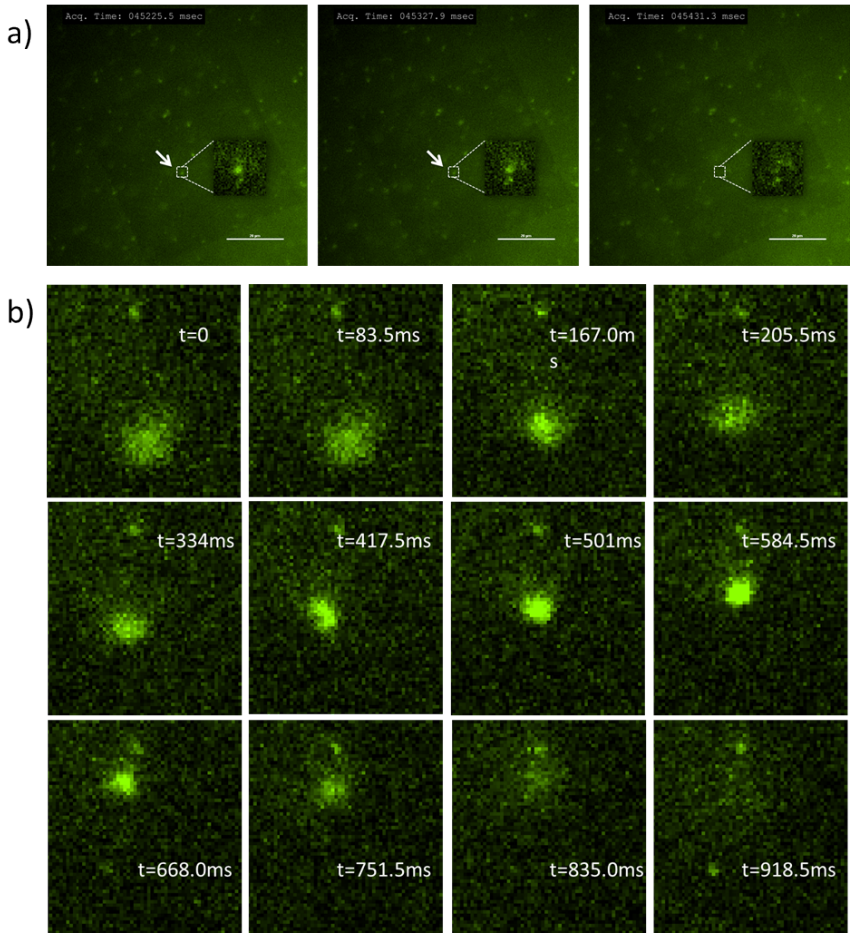

Figure 4.7 Optical observation of single DNA molecules through a nanopore. a) A molecule translocates through the nanopore, it approaches and then it is removed from the field of view. b) Close up view of the molecule translocation. The molecule approaches the pore and changes configurations until it is finally absorbed and no fluorescence is seen. Hundreds of events like this were observed at the pore location. Device B09.5 with a 10nm pore drilled with light enhanced dielectric breakdown. The molecules are lambda DNA, 48.9 kbp long stained with YOYO-1 dye (10base pairs / YOYO1 molecule) in 100mM KCl.

The electrical signal for this experiment was noisy (Figure 4.8) and does not provide information about the DNA translocation. Just from the optical signal, it is not clear when the translocation happened, that is, to what video frame the translocation corresponds. One could think that at t=584.5ms the molecule is concentrated in the smallest region. In any case, translocation takes ~0.1-1ms and

will either happen during the time when the camera is exposing (31ms) or during data transmission (~3ms) At this frame rate we cannot detect optically when translocation happens, hence the importance of the electrical measurements.

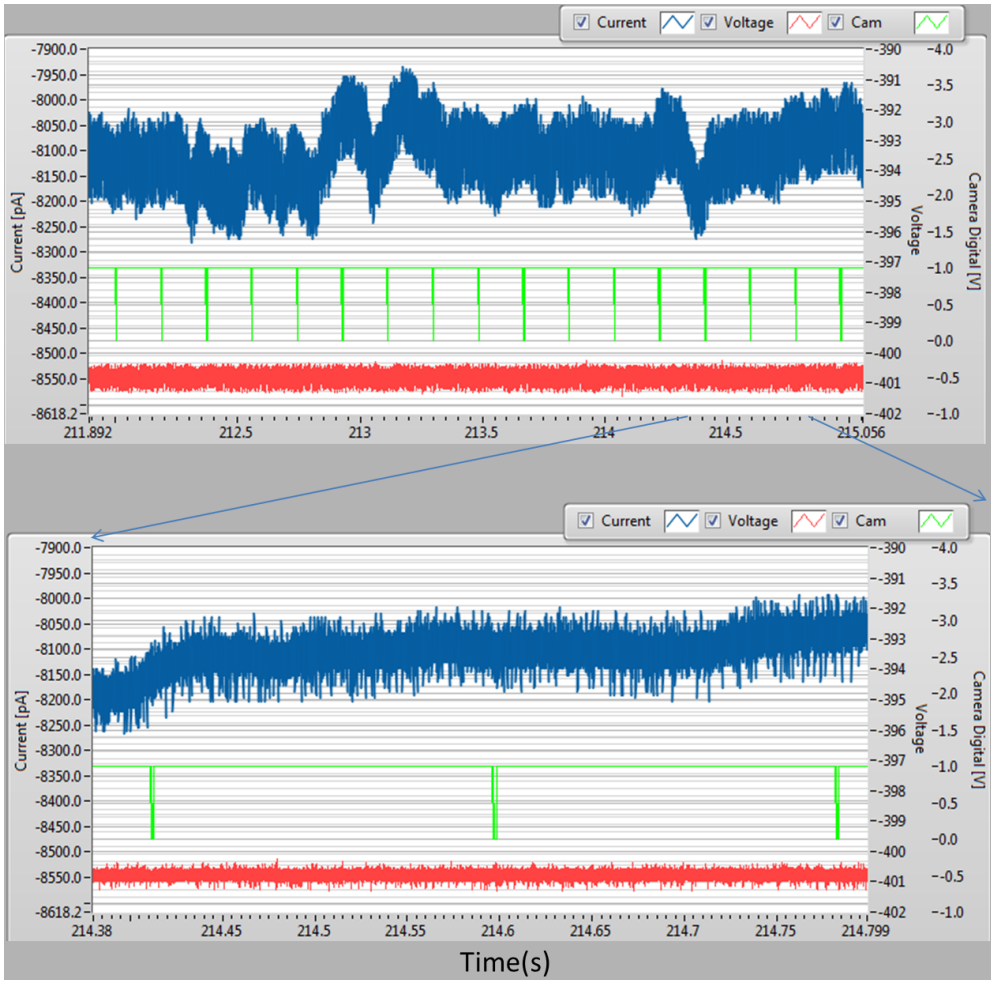

Figure 4.8 Synchronization. Synchronized electrical signal in blue, voltage shown in red and camera signal in green for the same experiment depicted in **Figure 4.7**. The green curve is 1V when the camera is exposing and 0 when not. At this point of the instrument´s development the laser caused a lot of noise and it was not possible to resolve the translocations that were detected optically.

The dynamics of capture and movement outside of the nanopore can be resolved with a precision determined by the frame rate. All the goals that we set in the introduction about measuring the polymer before translocation can be accomplished with the optical channel. The only limitation is the temporal resolution of the camera. For the video taken on this experiment it is 31fps, however, if a fraction of the camera sensor is used, the resolution can be brought to 7,980 fps (according to the vendor). That is, one frame each 0.12ms.

At this point, a major flaw of the instrument was its high noise current. But it was optimized as described in Chapter 3. I will now present the results with the electrical noise optimized.

4.3 Synchronous Electrical and Optical measurements

To detect DNA Optically and electrically with ease, we need DNA with covalently attached fluorophores, that is, fluorophores that have a strong bond to the DNA, so that they are stable under a wide range of electrolyte concentration. We are in the process of developing such fluorescently labelled DNA. However, I can do a control experiment in which I detect DNA electrically with all the optical system functioning, that is, in the same conditions as an Optical and Electrical experiment would be performed. Such an experiment will be the measure of the ability of the nanopore based optofluidic instrument to do simultaneous optical and electrical detection.

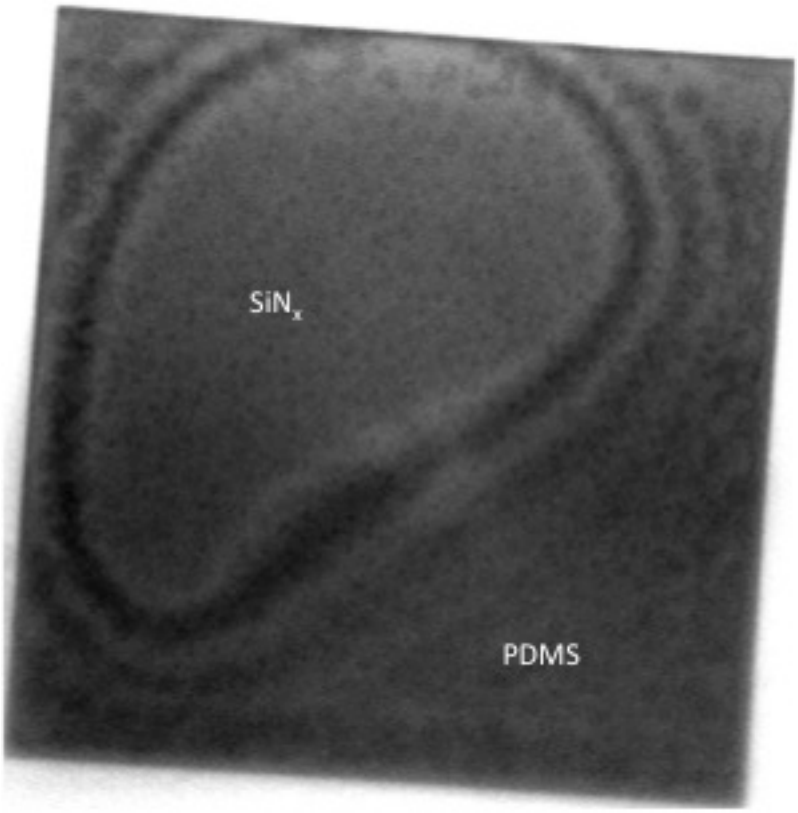

Figure 4.9 PDMS painted on the free standing membrane. Device B12.1 PDMS was painted on all over the chip, except on a region from the free-standing membrane. Only the region of the membrane shown in the picture is exposed to the solution.

As explained in Chapter 3, I was able to eliminate the coupling noise from the laser with the nanopore sensor by reducing the exposed area of the chip to the solution (Figure 4.9)

If only the silicon nitride is in contact with the electrolytic solution, this noise is not present anymore. At 10kHz the I_{rms} noise is 10pA, which gives us the possibility to readily detect DNA. The DNA signals are on the order of ~600pA in 3.6M LiCl, so the SNR will be 60 (Figure 4.10). But even in 100mM KCl, the maximum noise at

which detection should be possible is I_{rms}=37pA (detection should be possible even if noise increases by a factor of 4 due to the low electrolyte concentration).

As discussed in Chapter 3, painting PDMS on the membrane reduces the noise to such a level that is difficult to distinguish between the noise when the membrane is illuminated or not. Furthermore, the noise is practically independent of the illumination intensity.

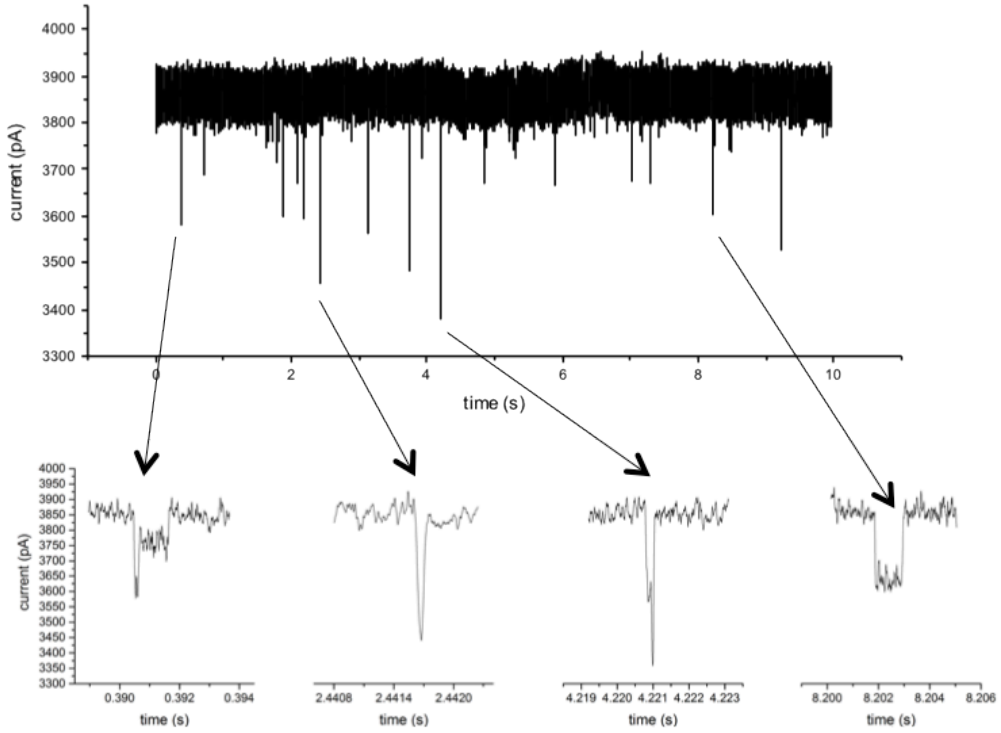

Figure 4.10 Electrical detection of 5kbp DNA with the optical system functioning. Trace of the current taken with the laser shining at 8mW on the membrane. Individual translocations are shown below. Device B12.1 with a 6 nm pore, on a 30nm membrane. Experiment done in 3.6M LiCl at 400mV with 5kbp DNA. Camera is off; to see results with the camera functioning, see **Figure 4.12**.

In the experiment 404 translocation events were detected in the selected sampling time. A change in conductance was measured for each one of them and plotted in Figure 4.11. The measurement average conductance change of all translocations is 0.81nS, which is low, compared to 1.87nS predicted by equation 1.3 (using l=30nm,

σ=14.78S/m, d_{DNA}=2.2nm). One also observes variability in both, the conductance change and the dwell time, compared to other nanopore experiments in standard setups (with no optics involved). There are several possible explanations for this variability. An illuminated nanopore has been shown to alter DNA dwell times[45] due to an alteration in the surface charge of the nanopore walls, the pores also were reported to experience a change in conductance. Finally, the thickness of the silicon nitride is also subject to 20-30% change from the vendor value, which will influence the calculated value for the conductance blockage.

Once again, this experiment raises interesting questions and opens future research possibilities, which was its initial goal.

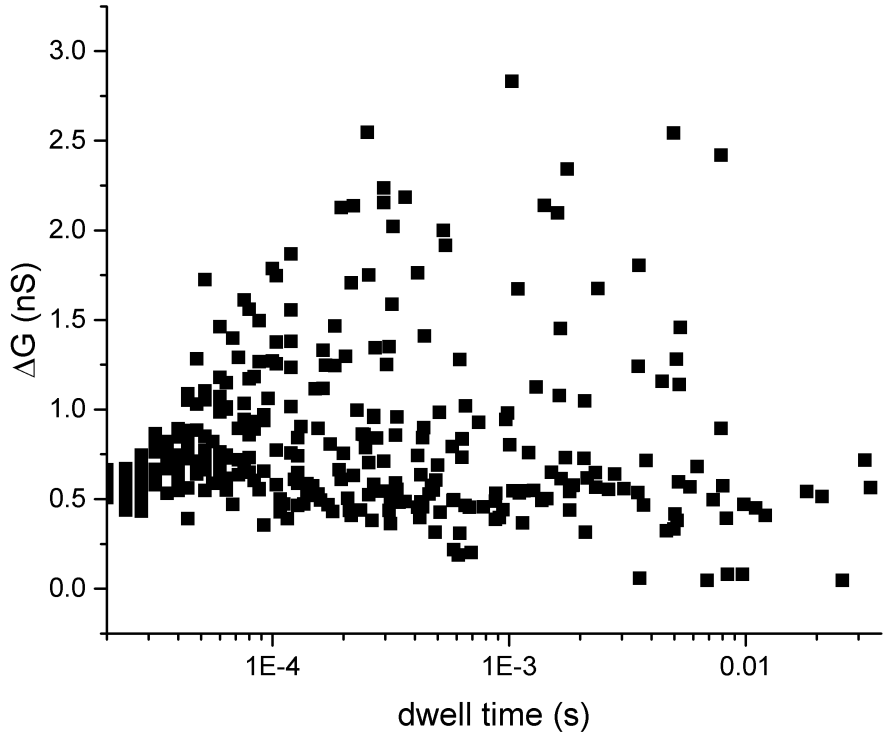

Figure 4.11 Conductance change as a function of dwell time. Scatter plot of the Conductance Change of the translocation events seen in the synchronous experiment (some traces are shown in the figure above). Device B12.1 with a 6nm pore, PDMS painted on the membrane. 5kbp DNA used in 3.6M LiCl solution.

4.4 Outlook

So far, I have presented the design, construction and optimization of a nanopore based optofluidic device capable of synchronous optical and electrical measurements. The tool that would render possible the interrogation of nanopore experiments with an optical and electrical channel is now ready to work. I hope it will be able to answer the open questions related to anomalous events, understand

clogging mechanism, and that it will be used to study the correlation between the conformation of DNA before translocation and the distribution of translocation times.

Additionally, during the development of the instrument a novel technique to fabricate nanopores on a defined location was developed.

I will now describe the steps that need to be taken in order to continue towards answering the questions that motivated the development of this tool, and I will also show the preliminary data on pore localization.

4.4.1 Fluorescently label DNA

In order to work at high salt concentrations where the signal is higher compared to the noise, the fluorophores need to be stable in such salt concentrations. This process can be done via PCR, but apparently the process has to be optimized in several ways. This fluorescently labelled DNA would be of tremendous help for the experiments.

4.4.2 Reduction of the noise coupling between the Camera and the DAQ card

As seen in the last section, the electrical signal noise is at an acceptable level. Nevertheless, there are minor further improvements to keep reducing the noise on the electrical signal. There is an electrical noise coupling between the synchronization signal from the camera and the current signal in the amplifier. In

the past, these issues have been related to the DAQ card multiplexing system (reading multiple channels). The current DAQ card features time multiplexing, that is, it uses the same sensor to measure multiple channels, so there is a minute charge transfer from one channel into the other. The solution to this issue is simply to have the DAQ card sample on an extra grounded channel, so that it discharges after sampling each channel, or to implement a DAQ card with independent channels.

The effect of the camera noise coupling can be seen in Figure 4.12. Noise is evident but nowhere near the level of a DNA signal. It is related to exposure time, as seen in Chapter 3.

Nevertheless, even if we include the noise from the camera, the I_{rms} noise is not greater than 15pA at 10kHz, which translates to a SNR of 40. This is a very promising scenario, and it could very well be possible to even detect DNA-YOYO1 complexes in 100mM KCl, with an expected current blockage of 150pA.

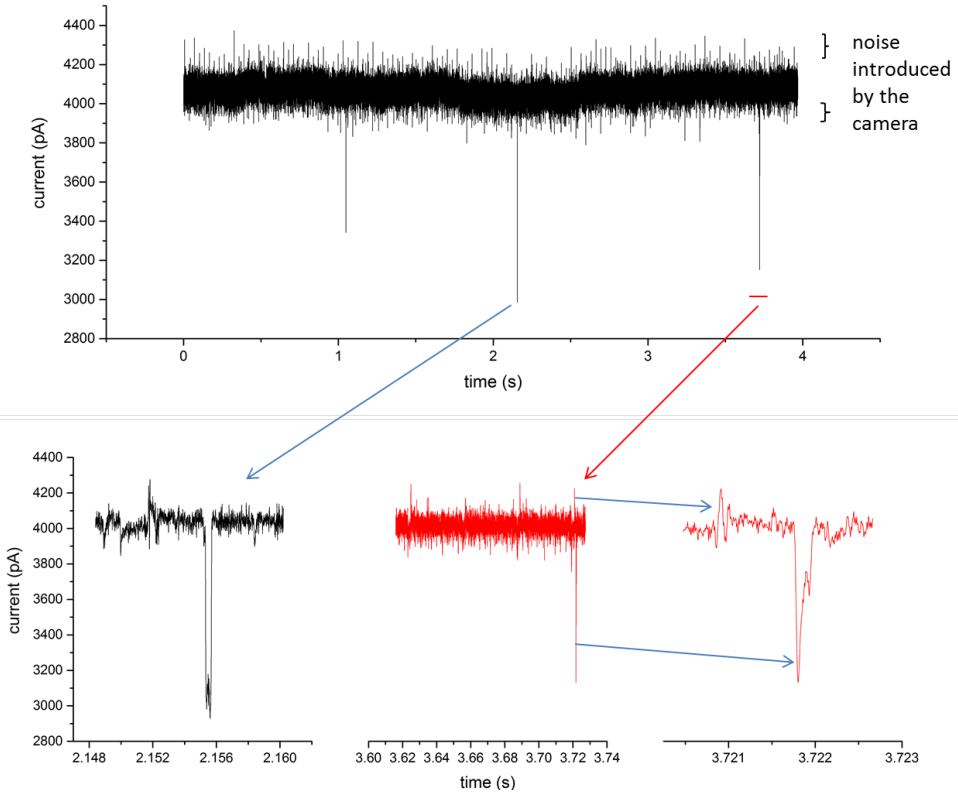

Figure 4.12 Translocation traces when both the camera and the laser are on. The camera produces upward going spikes, which influence the noise performance. Device B12.1 at 400mV data filtered at 10kHz by a hardware Bessel filter. Laser on, 8mW of power, Camera exposing at 30ms, 31 fps.

4.4.3 Increase of the temporal resolution of the optical channel

Increasing the temporal resolution of the Camera should be as simple as to change the acquisition parameters. However, that change might bring additional complications such as an increase in the coupling noise. Also, since the image size has to be reduced to increase the acquisition speed, the field of view will also be reduced. That should not affect the measurements since we are interested in a region in the vicinity of the nanopore (d=10µm).

4.5 Localized nanopore fabrication via laser enhanced dielectric breakdown

In the development of this instrument I have had some advantages with respect to traditional TEM drilled pores. I implemented the *in situ* creation method via Controlled Dielectric Breakdown[11] which facilitated the design of the system. A seeming disadvantage of the method is the random location of the pores, which will be created on the weakest spot on the membrane. I overcame this challenge, demonstrating controlled fabrication of the pore in one particular location. The method consists of locally increasing the conductivity of the desired spot by illuminating the area with a focused laser beam.

4.5.1 Theory

Given the capabilities of our instrument, we can utilize the fact that electrons-hole pairs are generated in SiN_x upon illumination with a light source as mentioned in chapter 3; the band gap of silicon nitride can allow the generation of electron hole pairs upon illumination with our 488nm laser. If the laser is focused on one particular spot, this location will be favoured in terms of conductivity with respect to the rest of the membrane, and the pore will be fabricated there, since the leakage current will be enhanced.

Other effects such as local heating can be discarded due to the low absorbance of water and SiN_x [45], at this particular wavelength and relatively low laser power used.

4.5.2 Beam focusing

The resolution of the method will be limited by the ability to focus the laser beam on a particular spot. For a proof-of-principle demonstration that this method can work, I only needed to find a way to focus the beam on a point to enhance the conductivity of that particular spot. This was accomplished with the inverse telescope used to expand the laser beam to fit into the port of the microscope. The telescope is normally positioned so that the incident and transmitted beam are collimated. Changing the distance between the two lenses can reduce the illumination region, until a diffraction-limited spot is formed.

Initially, a diffraction-limited spot was difficult to create. In fact, the first experiment shown in Figure 4.13 shows how the beam hits in almost all the membrane, which is 50μmx50μm in size. In spite of this, the laser beam is Gaussian and there was a privileged point at the centre of the beam, which would receive the highest intensity of light where the pore was indeed created.

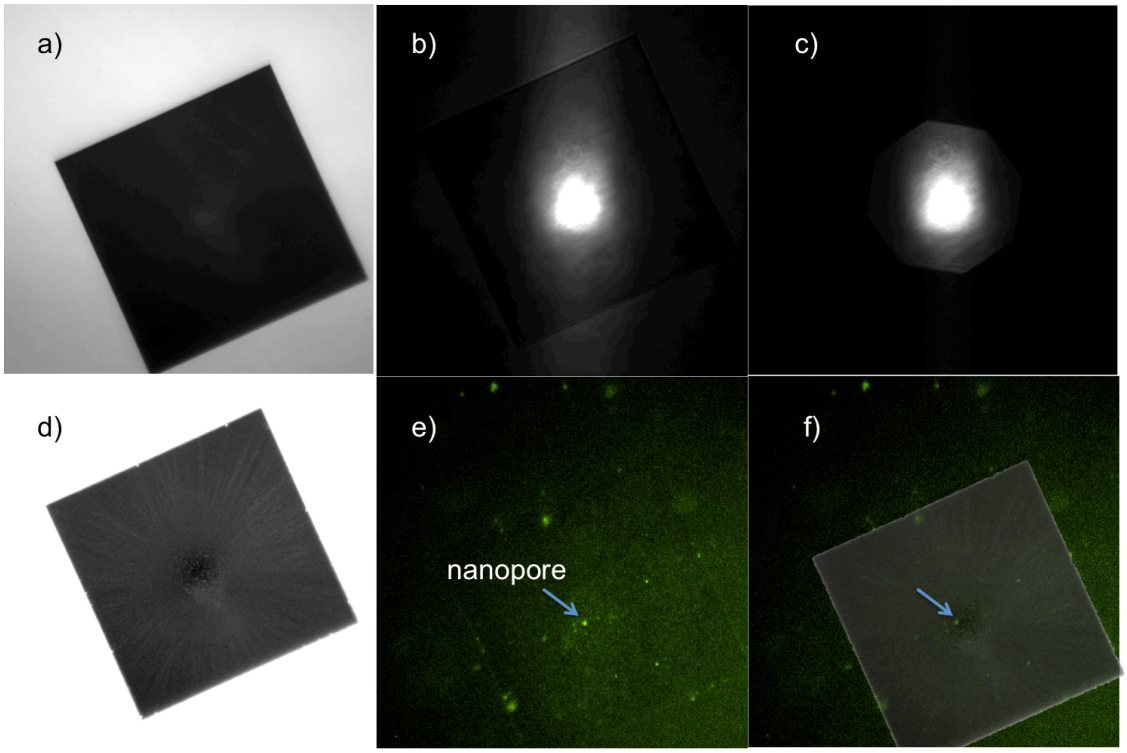

Figure 4.13 Creation of a nanopore with Localized laser enhanced dielectric breakdown. a) Picture of the membrane before creation b) laser shining at the membrane c) a diaphragm was used to assure light was reaching the silicon nitride membrane only d) image of the membrane after the pore fabrication. e) after a fluorescence experiment was carried out, the nanopore clogged and revealed its location, it is indeed located where the laser was hitting f) Images d) and e) superimposed revealing the correlation between the features created on the membrane and the final pore position. Device B09.5

However, I was able to focus the beam better if the beam expansion was done before the laser beam was reflected on the mirrors of the periscope. The illumination spot was reduced to 1.1µm, which is close to the theoretical diffraction limit of 192.1nm, considering imperfections of the optics.

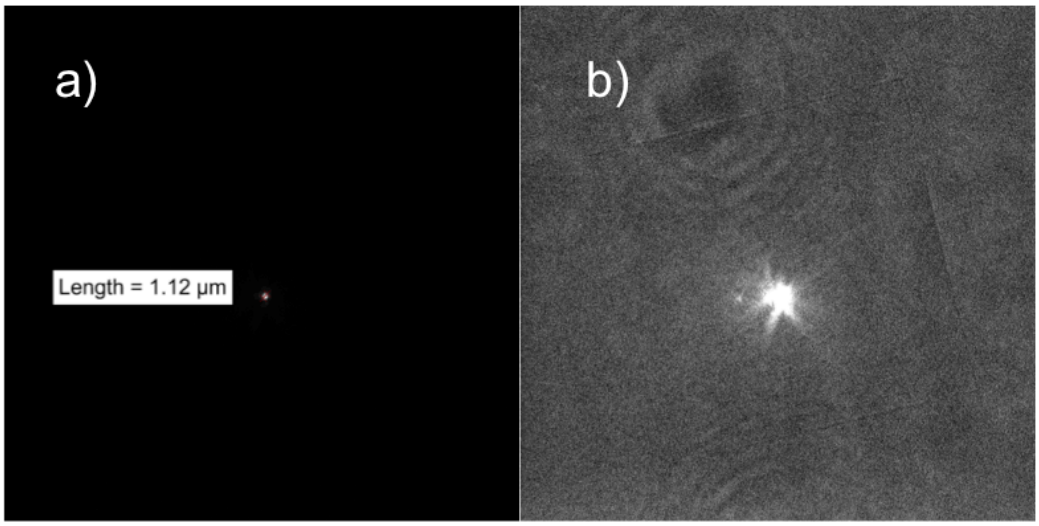

Figure 4.14 Laser focused on a very small spot. Laser focused on the membrane. a) Picture showing intensities from 0 to 1000 a.u. b) The same picture showing intensities from 0 to 20 a.u. so that the membrane is seen. This image was taken with a power of 0.1mW. The creation is performed at 30mW.

4.5.3 Current Increase upon the application of a focused beam

The increase in tunnelling current upon illumination is evidence that the localized dielectric breakdown is caused by photoconductivity. Figure 4.15 illustrates this phenomenon. It shows a plot of the voltage applied to a membrane and its current response in the dark, and the same voltage applied to the same membrane with the laser shining on a very small spot. At high voltages (>5V) the difference is significant.

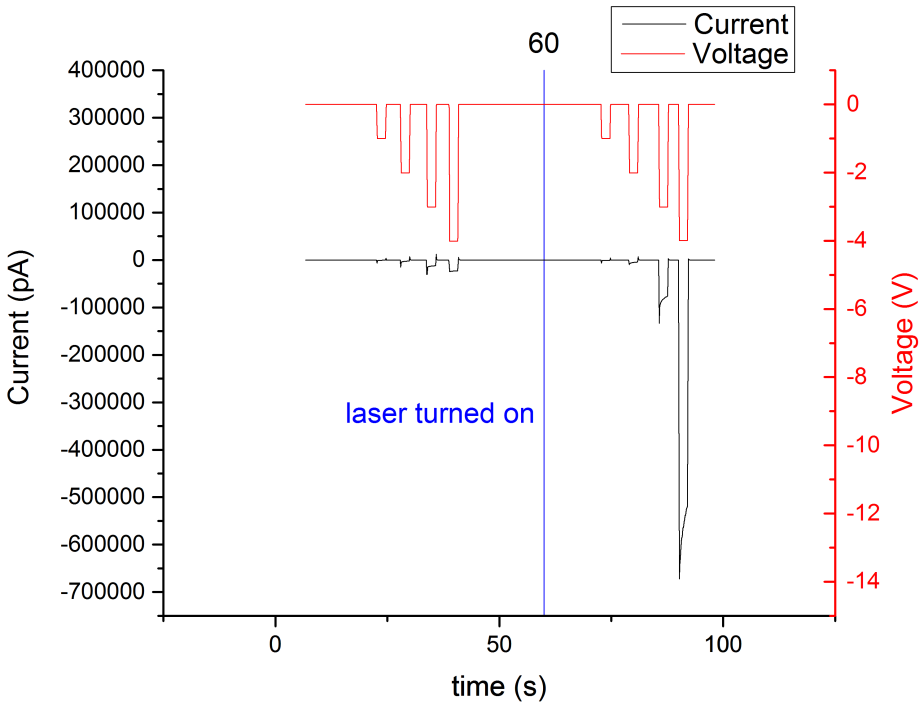

Figure 4.15 Tunnelling current through a blank membrane (with no pore). On the right we see the current upon the application of 4 voltage pulses when the membrane is not illuminated with a focused laser beam. On the right, the same voltages are applied but the laser is on, with a power of 30mW. The current increases significantly when the laser is illuminating. The photoconductivity of small region is responsible for the creation of a pore in that favoured location.

5 APPENDIX: SYNCHRONIZATION AND PROCEDURES

In this section, I will include details about the instrument. I will discuss synchronization and I will provide the detailed protocols of Device fabrication, DNA staining and mounting of the device for a DNA experiment.

5.1 Synchronization of Optical and Electrical measurements

In order to have synchronous optical and electrical measurements, a precise time signature had to accompany each one of the images taken by the camera. Conveniently, the camera Andor iXon 897 has a trigger output: a connector that will indicate when the camera is exposing with a digital voltage signal: it will be at 1V when the camera is exposing and it will drop to 0V when it is not. I connected

this terminal to the DAQ card, and the data is acquired simultaneously as the voltage and current signals, as can be seen on the Figure below.

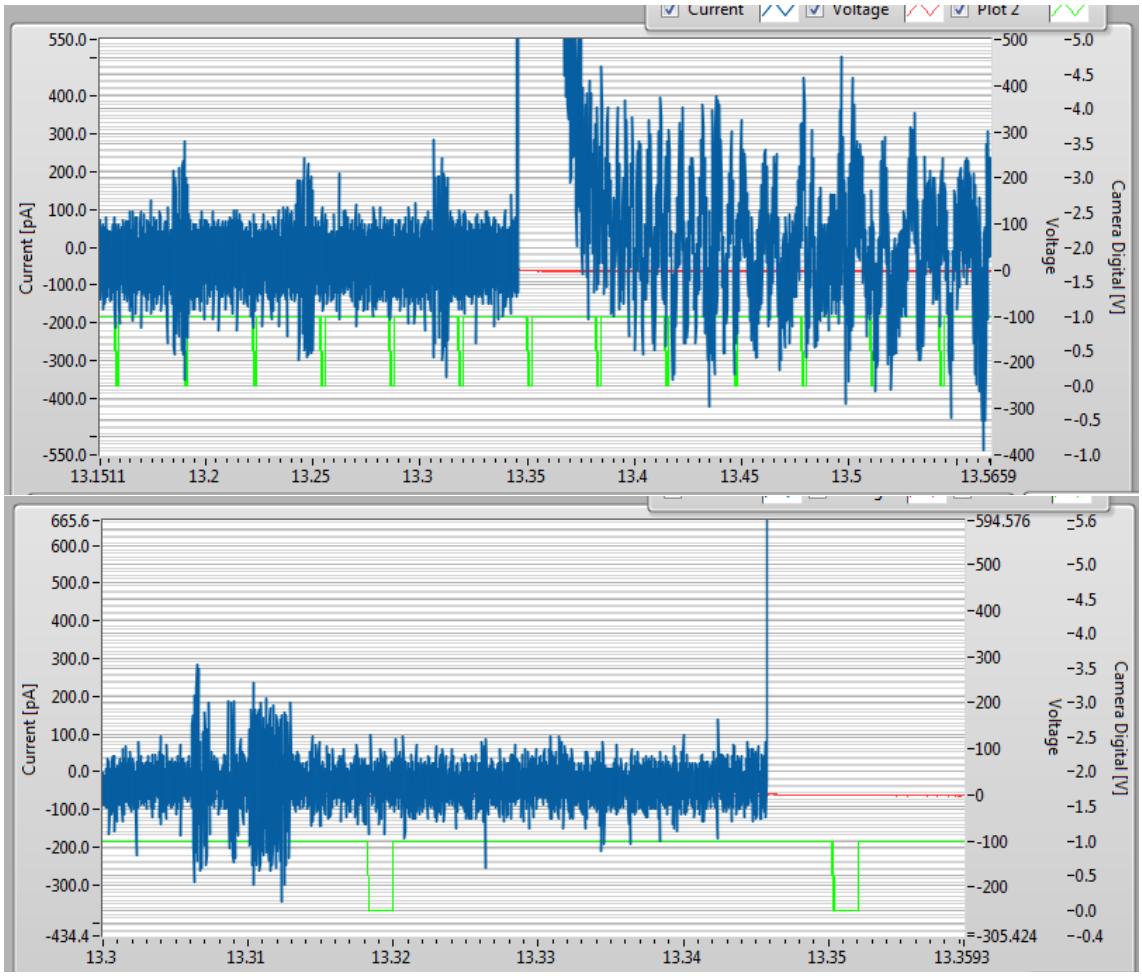

Figure 5.1 Synchronization of the electrical and Optical setup. A laser pulse is sent to the membrane and it produces two distinct signatures in the optical and electrical systems: there is a spike on the current, and an increase in optical intensity is observed in the frame at which illumination happened. The synchronization is acceptable within the time resolution of the camera.

5.2 Procedures and methods

I will describe the relevant procedures to get the instrument working. Namely, I will explain in detail how to fabricate a microfluidic device, the method to stain DNA and device preparation before an experiment.

5.2.1 Microfluidic Device Fabrication

This is the step-by-step protocol to manufacture microfluidic devices:

1. Making of PDMS Moulds
    a. Coat the machined aluminium moulds with trichlorosilane:
        i. Pour 10μL of trichlorosilane in a small petri dish.
        ii. Put the petri dish in a vacuum chamber along with the moulds.
        iii. Pump for 2 minutes.
        iv. Close the valve of the vacuum chamber and wait 1 hour for the trichlorosilane to coat the surface of the moulds. Use the Aluminium moulds and repeat the procedure after 7 PDMS moulds are fabricated or as needed.
    b. Prepare 1:5 PDMS (for 7 moulds usually 8 g is enough).
        i. Pour the elastomer and the curing agent in a tube, mix thoroughly for 10-15 minutes.
        ii. Ensure there is a vertical and horizontal mixing of the PDMS.
    c. Pour the PDMS over the moulds and scoop the surface with a glass slide to level the PDMS horizontally.

d. Leave in an oven for 2 hours at 80° C
e. Remove the PDMS from the Al mould carefully.
f. Punch a 3mm hole with the 3mm hole puncher on the centre of the square intrusion of the PDMS moulds.

2. Making of thin 1:10 PDMS films
    a. Prepare 7g of 1:10 PDMS, in a tube and mix thoroughly (see 1.b).
    b. Coat the master wafer with trichlorosilane (see 1.a).
    c. Verify that the PDMS is cured.
    d. Take the master wafer, the 1:10 PDMS, to the clean room.
    e. Spin coat the PDMS on to the master wafer. Use 600 rpm for 90 s with ramp speed of 133 rpm/s to obtain 100um thickness.[53]
    f. Put the master wafer in an oven for 2 hours at 80 °C.
3. Bonding of the thin PDMS films to moulds.
    a. Clean the moulds with Ethanol, Methanol and Isopropanol. It is better to rinse them in the clean room just before plasma cleaning.
    b. Plasma clean the mould and the film (still covering the wafer) for 30s at 30W.
    c. Place the mould over the master wafer with the PDMS film using the alignment marks to position the PDMS mould properly. The most important aspect is to place the pillars of the

PDMS mould on top of the channel endings. It is not necessary to use the mask aligner, hand positioning is usually acceptable.

   d. Repeat steps 3a, and 3b until all the PDMS moulds are bonded to the thin film on the wafer.
   e. Cure in the oven for 2 hours.

4. Detaching the bonded PDMS moulds and film from the wafer
   a. Cut the PDMS film around the PDMS moulds with a scalpel, trying to not damage the features of the master wafer.
   b. Peel the bonded moulds from the wafer (the moulds should come off with the film below them).
5. Punching holes on the Bonded Mould/Film
   a. Punch holes on the columns with a 0.75mm hole puncher.
   b. Punch one hole on the centre of the membrane with a 1mm puncher (punching with a smaller hole puncher might be beneficial for the noise performance, and might reduce leakage current during nanopore fabrication).
6. Bonding the Mould/Film to the cover slip
   a. Rinse the Mould/Film and the coverslip with Ethanol, Methanol and Isopropanol.
   b. Plasma clean the Mould/Film and the coverslip for 30s at 30W.
   c. Bond them together. Push bubbles away with tweezers trying to make a good contact between the PDMS and the glass. We will

refer to the PDMS mould+ Film+ cover slip as the "microfluidic device".

7. Bond the nanopore chip
    a. Rinse device if necessary with Ethanol, Methanol and Isopropanol. Dry it with nitrogen.
    b. Plasma clean the device for 60s at 60W, and the chip simultaneously. Use a PDMS chip holder to hold the chip.
    c. Carefully place the chip on the stereomicroscope. Carefully approach the chip with the microfluidic device from the top until contact is made. PDMS binds very fast to chips. One has only one chance per device.
        i. If the chip was previously painted with PDMS, the same protocol should be used (with the exception that 30W for 30s are used). PDMS should be painted again at the etched pit side to ensure no leaks are present between both sides of the nanopore chip.
    d. Repeat with all other moulds.
8. Bonding of PDMS slab to the back of the chip.
    a. Cut and punch two holes on a PDMS slab.
    b. Plasma clean the slab and the device for 30s and 30W.
    c. Bond the PDMS slab to the back of the device to have the finalized device as seen in Figure 2.5
9. Cure the device in the oven for 2 hours.

a. The microfluidic device is ready for experiments.

5.2.2 DNA staining with YOYO-1 dye

1. Make the appropriate YOYO-1 dilutions to have 1 YOYO-1 molecule per 10 bp - 50bp gives a good optical signal.
2. Mix the DNA and the YOYO-1 solutions in DI water.
3. Incubate for 90 minutes at 40 ° C.
4. Rinse with cold water and store at 4 ° C.
5. At this point the DNA can be mixed with 100mM solution. Store the stained DNA at 4 °C.

6 REFERENCES

1. Merchant, C. A. *et al.* DNA translocation through graphene nanopores. *Nano Lett.* **10,** 2915–2921 (2010).

2. Siwy, Z. & Fuliński, A. Origin of 1/f^{α} Noise in Membrane Channel Currents. *Phys. Rev. Lett.* **89,** 1–4 (2002).

3. Bezrukov, S. M., Vodyanoy, I. & Parsegian, V. A. Counting polymers moving through a single ion channel. *Nature* **370,** 279–281 (1994).

4. Deamer, D. W. & Branton, D. Characterization of nucleic acids by nanopore analysis. *Acc. Chem. Res.* **35,** 817–25 (2002).

5. Meller, A. Dynamics of polynucleotide transport through nanometre-scale pores. *J. Phys. Condens. Matter* **15,** 581–607 (2003).

6. Lu, B., Albertorio, F., Hoogerheide, D. P. & Golovchenko, J. a. Origins and consequences of velocity fluctuations during DNA passage through a nanopore. *Biophys. J.* **101,** 70–9 (2011).

7. Larkin, J. *et al.* Slow DNA Transport through Nanopores in Hafnium Oxide Membranes. *ACS Nano* (2013). doi:10.1021/nn404326f

8. Hoogerheide, D., Albertorio, F. & Golovchenko, J. Escape of DNA from a Weakly Biased Thin Nanopore: Experimental Evidence for a Universal Diffusive Behavior. *Phys. Rev. Lett.* **111,** 248301 (2013).

9. Branton, D. *et al.* The potential and challenges of nanopore sequencing. *Nat. Biotechnol.* **26,** 1146–1153 (2008).

10. Gibb, T. & Ayub, M. in *Eng. Nanopores Bioanal. Appl.* (Edel, J. B. & Albrecht, T.) 121–140 (Norwich, N.Y. : William Andrew ; Oxford : Elsevier Science distributor, 2013). doi:10.1016/B978-1-4377-3473-7.00005-4

11. Kwok, H., Briggs, K. & Tabard-Cossa, V. Nanopore fabrication by controlled dielectric breakdown. *PLoS One* **9,** e92880 (2014).

12. Firnkes, M., Pedone, D., Knezevic, J., Döblinger, M. & Rant, U. Electrically facilitated translocations of proteins through silicon nitride nanopores: conjoint and competitive action of diffusion, electrophoresis, and electroosmosis. *Nano Lett.* **10,** 2162–7 (2010).

13. Beamish, E., Kwok, H., Tabard-Cossa, V. & Godin, M. Fine-tuning the Size and Minimizing the Noise of Solid-state Nanopores. *J. Vis. Exp.* e51081 (2013). doi:10.3791/51081

14. Dobrucki, J. W. in *Fluoresc. Microsc. From Princ. to Biol. Appl.* (Kubitscheck, U.) 107–142 (Wiley-VCH Verlag GmbH & Co. KGaA, 2013). at <http://dx.doi.org/10.1002/9783527671595.ch3>

15. Berard, D. *et al.* Precision platform for convex lens-induced confinement microscopy. *Rev. Sci. Instrum.* **84,** 103704 (2013).

16. Zhang, K. & Luo, K. Polymer translocation into a confined space: influence of the chain stiffness and the shape of the confinement. *J. Chem. Phys.* **140,** 094902 (2014).

17. Soni, G. V *et al.* Synchronous optical and electrical detection of biomolecules traversing through solid-state nanopores. *Rev. Sci. Instrum.* **81,** 014301 (2010).

18. McNally, B. *et al.* Optical recognition of converted DNA nucleotides for single-molecule DNA sequencing using nanopore arrays. *Nano Lett.* **10,** 2237–2244 (2010).

19. Smeets, R. M. M. *et al.* Salt Dependence of Ion Transport and DNA Translocation through Solid-State Nanopores. *Nano Lett.* **6,** 89–95 (2006).

20. Kurz, V., Nelson, E. M., Shim, J. & Timp, G. Direct Visualization of Single-Molecule Translocations through Synthetic Nanopores Comparable in Size to a Molecule. *ACS Nano* **7,** 4057–69 (2013).

21. Ando, G., Hyun, C., Li, J. & Mitsui, T. Directly observing the motion of DNA molecules near solid-state nanopores. *ACS Nano* **6,** 10090–10097 (2012).

22. Kowalczyk, S. W., Grosberg, A. Y., Rabin, Y. & Dekker, C. Modeling the conductance and DNA blockade of solid-state nanopores. *Nanotechnology* **22,** 315101 (2011).

23. Li, J. & Talaga, D. S. The distribution of DNA translocation times in solid-state nanopores. *J. Phys. Condens. Matter* **22,** 454129 (2010).

24. Tabard-Cossa, V. in *Eng. Nanopores Bioanal. Appl.* (Edel, J. B. & Albrecht, T.) 59–93 (Norwich, N.Y. : William Andrew ; Oxford : Elsevier Science distributor, 2013). doi:10.1016/B978-1-4377-3473-7.00003-0

25. Murphy, Douglas B. and Davidson, M. W. in *Fundam. Light Microsc. Electron. Imaging* 103–113 (John Wiley & Sons, Inc., 2012).

26. Murphy, Douglas B. and Davidson, M. W. in *Fundam. Light Microsc. Electron. Imaging* 153–171 (John Wiley & Sons, Inc., 2012).

27. Whitesides, G. M., Ostuni, E., Takayama, S., Jiang, X. & Ingber, D. E. Soft lithography in biology and biochemistry. *Annu. Rev. Biomed. Eng.* **3,** 335–373 (2001).

28. Cosa, G., Focsaneanu, K. S., McLean, J. R., McNamee, J. P. & Scaiano, J. C. Photophysical properties of fluorescent DNA-dyes bound to single- and double-stranded DNA in aqueous buffered solution. *Photochem. Photobiol.* **73,** 585–99 (2001).

29. Tabard-Cossa, V., Trivedi, D., Wiggin, M., Jetha, N. N. & Marziali, A. Noise analysis and reduction in solid-state nanopores. *Nanotechnology* **18,** 305505 (2007).

30. Smeets, R. M. M., Dekker, N. H. & Dekker, C. Low-frequency noise in solid-state nanopores. *Nanotechnology* **20,** 095501 (2009).

31. Howard, R. M. *Principles of random signal analysis and low noise design the power spectral density and its applications*. (John Wiley & Sons., 2002). at <http://ieeexplore.ieee.org/servlet/opac?bknumber=5236635>

32. Bezrukov, S. M. & Winterhalter, M. Examining Noise Sources at the Single-Molecule Level: 1/f Noise of an Open Maltoporin Channel. *Phys. Rev. Lett.* **85,** 202–205 (2000).

33. Wohnsland, F. & Benz, R. Membrane Biology 1 / f-Noise of Open Bacterial Porin Channels. **85,** 77–85 (1997).

34. Smeets, R. M. M., Keyser, U. F., Dekker, N. H. & Dekker, C. Noise in solid-state nanopores. *Proc. Natl. Acad. Sci. U. S. A.* **105,** 417–421 (2008).

35. Deen, M. J., Rumyantsev, S. L. & Schroter, M. On the origin of 1/f noise in polysilicon emitter bipolar transistors. *J. Appl. Phys.* **85,** 1192 (1999).

36. Smeets, R. M. M., Keyser, U. F., Wu, M. Y., Dekker, N. H. & Dekker, C. Nanobubbles in Solid-State Nanopores. *Phys. Rev. Lett.* **97,** 1–4 (2006).

37. Tabard-Cossa, V. in (2013). at <http://store.elsevier.com/Engineered-Nanopores-for-Bioanalytical-Applications/Joshua-B_-Edel/isbn-9781437734737/>

38. The Axon Guide - Electrophysiology and Biophysics Laboratory Techniques. (Molecular Devices, 2012).

39. Benndorf, K. *Single-Channel Recording; Chapter 5: Low-Noise Recording*. 129–145 (Springer US, 2009). doi:10.1007/978-1-4419-1229-9

40. Levis, R. a & Rae, J. L. The use of quartz patch pipettes for low noise single channel recording. *Biophys. J.* **65,** 1666–77 (1993).

41. Sigworth, F. J. & Colquhoun, D. *Single-Channel Recording; Chapter 19: Fitting and Statistical Analysis of Single Channel Records*. 483–587 (Springer US, 2009). doi:10.1007/978-1-4419-1229-9

42. Robertson, J. & Powell, M. J. Gap states in silicon nitride. *Appl. Phys. Lett.* **44,** 415 (1984).

43. Robertson, J., Warren, W. L. & Kanicki, J. Nature of the Si and N dangling bonds in silicon nitride. *J. Non. Cryst. Solids* **187,** 297–300 (1995).

44. Sze, S. M. & NG, K. K. *Physics of Semiconductor Devices*. (Willey-Interscience, 2007).

45. Di Fiori, N. *et al.* Optoelectronic control of surface charge and translocation dynamics in solid-state nanopores. *Nat. Nanotechnol.* **8,** 946–51 (2013).

46. Powell, M. R. *et al.* Nanoprecipitation-assisted ion current oscillations. *Nat. Nanotechnol.* **3,** 51–7 (2008).

47. Li, Y. *et al.* Harnessing plasmon-induced ionic noise in metallic nanopores. *Nano Lett.* **13,** 1724–1729 (2013).

48. Fiori, N. Di, Squires, A., Bar, D., Gilboa, T. & Moustakas, T. D. Supplementary information. 1–15 (2013). doi:10.1038/NNANO.2013.221

49. Sawafta, F., Clancy, B., Carlsen, A. T., Huber, M. & Hall, A. R. Solid-state nanopores and nanopore arrays optimized for optical detection. *Nanoscale* **6,** 6991–6 (2014).

50. Wanunu, M., Morrison, W., Rabin, Y., Grosberg, A. Y. & Meller, A. Electrostatic focusing of unlabelled DNA into nanoscale pores using a salt gradient. *Nat. Nanotechnol.* **5,** 160–165 (2010).

51. Nkodo, a E. *et al.* Diffusion coefficient of DNA molecules during free solution electrophoresis. *Electrophoresis* **22,** 2424–32 (2001).

52. Muthukumar, M. Theory of capture rate in polymer translocation. *J. Chem. Phys.* **132,** 195101 (2010).

53. Mata, A., Fleischman, A. J. & Roy, S. Characterization of polydimethylsiloxane (PDMS) properties for biomedical micro/nanosystems. *Biomed. Microdevices* **7,** 281–93 (2005).